


Bose-Hubbard triangular ladder in an artificial gauge field

Catalin-Mihai Halati  and Thierry Giamarchi 

Department of Quantum Matter Physics, University of Geneva, Quai Ernest-Ansermet 24, 1211 Geneva, Switzerland

 (Received 26 October 2022; revised 27 January 2023; accepted 27 January 2023; published 17 February 2023)

We consider interacting bosonic particles on a two-leg triangular ladder in the presence of an artificial gauge field. We employ density matrix renormalization group numerical simulations and analytical bosonization calculations to study the rich phase diagram of this system. We show that the interplay between the frustration induced by the triangular lattice geometry and the interactions gives rise to multiple chiral quantum phases. Phase transitions between superfluid to Mott-insulating states occur, which can have Meissner or vortex character. Furthermore, a state that explicitly breaks the symmetry between the two legs of the ladder, the biased chiral superfluid, is found for values of the flux close to π . In the regime of hard-core bosons, we show that the extension of the bond order insulator beyond the case of the fully frustrated ladder exhibits Meissner-type chiral currents. We discuss the consequences of our findings for experiments in cold atomic systems.

DOI: [10.1103/PhysRevResearch.5.013126](https://doi.org/10.1103/PhysRevResearch.5.013126)

I. INTRODUCTION

The interplay between kinetic energy and interactions leads, for quantum systems, to a very rich set of many-body phases with remarkable properties, such as superconductivity, or Mott insulators. This is particularly true in reduced dimensionality, where the effects of interactions are at their maximum. This leads in one dimension to a set of properties, known as Tomonaga-Luttinger liquids [1]. These are quite different from the typical physics that exists in higher dimensions, characterized by ordered states with single-particle-type excitations, such as Bogoliubov excitations for bosons or Landau quasiparticles for fermions.

An intermediate situation is provided by ladders, i.e., a small number of one-dimensional (1D) chains coupled by tunneling. Such systems possess some unique properties, different from both the one- and the high-dimensional ones. For example, fermionic ladders exhibit superconductivity with purely repulsive interactions, at variance with isolated 1D chains that are dominated by antiferromagnetic correlations [2].

Ladders are also the minimal systems in which the orbital effects of a magnetic field can be explored. For bosonic ladders this has allowed to predict [3] the existence of quantum phase transitions as a function of the flux between a low-field phase with current along the legs (Meissner phase) and a high-field phase with currents across the rungs and the presence of vortices (vortex phase), akin to the transition occurring in type II superconductors. Ultracold atomic systems offer the possibility of studying such systems coupled to artificial gauge fields [4,5], and the Meissner-to-vortex phase transition has been observed experimentally [6]. These works have paved

the way for a flurry of studies for other situations both for bosonic and fermionic ladders [3,7–30]. Furthermore, properties beyond the phase diagram, such as the Hall effect, were also studied [31,32] and even measured [33–35].

These extensive studies of ladders have, however, concentrated mostly on square ladders, for which the effect of hopping is unfrustrated, leaving the case of triangular ladders under flux relatively unexplored, despite some previous studies focusing on particular setups, or corners of the phase diagram [36–45]. The triangular structure is not bipartite and, thus, prevents the particle-hole symmetry that occurs naturally in square lattices. This has drastic consequences since it leads to frustration of the kinetic energy and, thus, to quite different properties, as was largely explored for two-dimensional systems [46–50].

In this paper, we explore the phase diagram of a triangular two-leg bosonic ladder under an artificial magnetic field. We consider bosons with a contact-repulsive interaction. We study, using a combination of analytical bosonization and numerical density matrix renormalization group (DMRG) techniques, the phase diagram of such a system as a function of the magnetic field, filling, and repulsion between the bosons. We discuss in particular our findings in comparison with the phases found for the square ladders.

The plan of the paper is as follows. In Sec. II we describe the model considered, its noninteracting limit and the observables of interest. In Sec. III we briefly discuss the methods employed in this work. We present the results regarding the phase diagram at half filling in Sec. IV. In this regime, we identify the following quantum phases: the Meissner superfluid (M-SF), the vortex superfluid (V-SF), and the biased chiral superfluid (BC-SF), which breaks the \mathbb{Z}_2 symmetry of the ladder. For the fully frustrated π -flux ladder (Sec. IV C), we obtain a transition between superfluid and chiral superfluid states. In the limit of hard-core bosons (Sec. V), at π flux we have successive phase transitions between superfluid, bond order insulator, and chiral superfluid states. The bond order extends in the phase diagram for lower values of the flux to

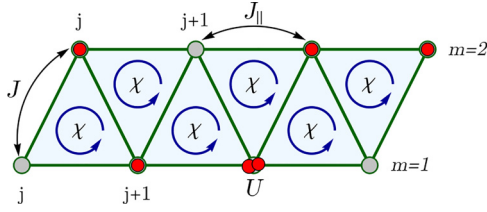


FIG. 1. Sketch of the setup. The bosonic atoms are confined in a quasi-one-dimensional triangular ladder. The legs are numbered by $m = 1, 2$ and the sites on each leg by j . The atoms tunnel along the legs with the amplitude J_{\parallel} , along the rungs with the amplitude J , and have an on-site interaction of strength U . Each triangular plaquette is pierced by a flux χ .

the chiral bond order insulator (C-BOI). At unity filling for interacting bosons (Sec. VI), also a Meissner Mott insulator (M-MI) can be found in the phase diagram. We discuss our results in Sec. VII and conclude in Sec. VIII.

II. MODEL

A. Setup

We consider interacting bosonic atoms confined to a triangular ladder in an artificial gauge field, as sketched in Fig. 1. The Bose-Hubbard Hamiltonian of the system is given by

$$\begin{aligned}
 H &= H_{\parallel} + H_{\perp} + H_{\text{int}}, \\
 H_{\parallel} &= -J_{\parallel} \sum_{j=1}^{L-1} (e^{-i\chi} b_{j,1}^{\dagger} b_{j+1,1} + e^{i\chi} b_{j,2}^{\dagger} b_{j+1,2} + \text{H.c.}), \\
 H_{\perp} &= -J \sum_{j=1}^L (b_{j,1}^{\dagger} b_{j,2} + \text{H.c.}) \\
 &\quad - J \sum_{j=1}^{L-1} (b_{j+1,1}^{\dagger} b_{j,2} + \text{H.c.}), \\
 H_{\text{int}} &= \frac{U}{2} \sum_{j=1}^L \sum_{m=1}^2 n_{j,m} (n_{j,m} - 1). \quad (1)
 \end{aligned}$$

The bosonic operator $b_{j,m}$ and $b_{j,m}^{\dagger}$ are the annihilation and creation operators of the particles at position j and leg $m = 1, 2$. We consider a total number of $N = \sum_{j=1}^L \sum_{m=1}^2 n_{j,m}$ atoms and that the ladder has L sites on each leg. The atomic density is given by $\rho = N/(2L)$. H_{\parallel} describes the tunneling along the two legs of the ladder, indexed by j , with amplitude J_{\parallel} . The complex factor in the hopping stems from the artificial magnetic field, with flux χ [4,5]. The tunneling along the rungs of the ladder is given by H_{\perp} and has amplitude J . The atoms interact repulsively with with an on-site interaction strength $U > 0$.

B. Noninteracting limit

In the noninteracting, $U = 0$, limit we can exactly diagonalize Hamiltonian (1) (see Appendix A) and obtain the

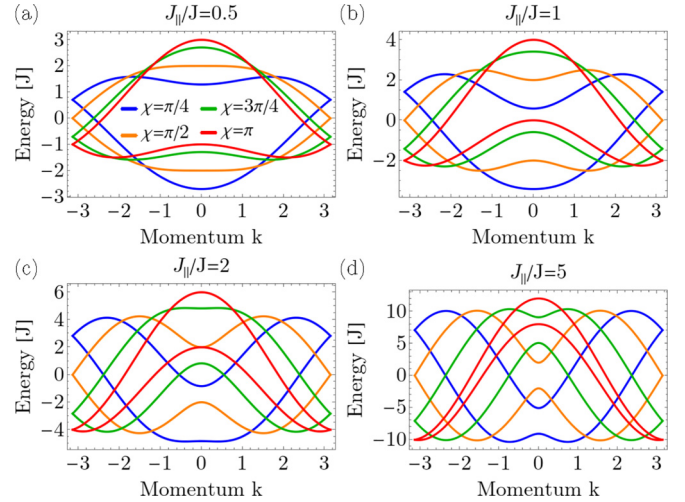


FIG. 2. Single-particle dispersion of model (1), $E_{\pm}(k)$ [Eq. (2)], as a function of momentum k , for (a) $J_{\parallel}/J = 0.2$, (b) $J_{\parallel}/J = 1$, (c) $J_{\parallel}/J = 2$, (d) $J_{\parallel}/J = 5$, and different values of the flux $\chi \in \{\pi/4, \pi/2, 3\pi/4, \pi\}$. Note the presence of the two minima away from $k = 0$ for some values of the flux and transverse hopping.

following dispersion relation:

$$\begin{aligned}
 E_{\pm}(k) &= -2J_{\parallel} \cos(k) \cos(\chi) \\
 &\quad \pm \sqrt{2J^2 [1 + \cos(k)] + 4J_{\parallel}^2 \sin^2(k) \sin^2(\chi)}. \quad (2)
 \end{aligned}$$

The noninteracting bands, $E_{\pm}(k)$, are represented in Fig. 2 for several values of J_{\parallel}/J and χ . We can observe that the lower band can have either a single minimum at $k = 0$, e.g., for Fig. 2(a) for $J_{\parallel}/J = 0.5$ and $\chi = 0.25\pi$, or two minima at finite values of k , e.g., for Fig. 2(c) for $J_{\parallel}/J = 2$ and $\chi = 0.5\pi$. The position of the double minima depends on J_{\parallel}/J and χ .

The topology of the lower band can already provide some hints regarding the nature of the ground state in the case of weakly interacting bosons. Similarly with the analysis performed in the case of the square ladder with flux [12,18] we expect phases of the following natures: Meissner states, in the case in which the bosons condense in the $k = 0$ minimum; vortex phases, in the case of two condensates in the two minima of the lower band; and states which break the \mathbb{Z}_2 symmetry of the ladder, corresponding to a condensate in just one of the double minima. In Secs. IV and VI we show how these states are realized on the triangular ladder in the interacting regime.

C. Observables of interest

In the rest of this section, we describe some of the observables which are suitable for the investigation of the chiral phases we obtain in this system. We define the local currents on the leg $j_{j,m}^{\parallel}$ and the rung j_j^{\perp} , respectively, as

$$\begin{aligned}
 j_{j,m}^{\parallel} &= -iJ_{\parallel} (e^{i\chi(-1)^m} b_{j,m}^{\dagger} b_{j+1,m} - \text{H.c.}), \\
 j_{2j-1}^{\perp} &= -iJ (b_{j,1}^{\dagger} b_{j,2} - \text{H.c.}), \\
 j_{2j}^{\perp} &= -iJ (b_{j+1,1}^{\dagger} b_{j,2} - \text{H.c.}). \quad (3)
 \end{aligned}$$

In addition to the local currents, the chiral current J_c and the average rung current J_r are of interest and defined as

$$J_c = \frac{1}{2(L-1)} \sum_j \langle j_{j,1}^{\parallel} - j_{j,2}^{\parallel} \rangle,$$

$$J_r = \frac{1}{2L-1} \sum_j |\langle j_j^{\perp} \rangle|. \quad (4)$$

In order to identify biased phases, in which the \mathbb{Z}_2 symmetry between the two legs of the ladder is broken, we compute the density imbalance

$$\Delta n = \frac{1}{2L} \sum_j (n_{j,1} - n_{j,2}). \quad (5)$$

Furthermore, we compute the central charge c , which can be interpreted as the number of gapless modes. We extract the central charge from the scaling of the von Neumann entanglement entropy $S_{vN}(l)$ of an embedded subsystem of length l in a chain of length L . For open boundary conditions the entanglement entropy for the ground state of gapless phases is given by [51–53]

$$S_{vN} = \frac{c}{6} \log \left(\frac{L}{\pi} \sin \frac{\pi l}{L} \right) + s_1, \quad (6)$$

where s_1 is a nonuniversal constant, and we neglect logarithmic corrections [54] and oscillatory terms [55] due to the finite size of the system.

III. METHODS

A. Bosonization

The low-energy physics of one-dimensional interacting quantum systems, corresponding to the Tomonaga-Luttinger liquids universality class, can be described in terms of two bosonic fields ϕ and θ [1]. These bosonic fields are related to the collective excitations of density and currents and fulfill the canonical commutation relation, $[\phi(x), \nabla\theta(x')] = i\pi\delta(x - x')$. In the bosonized representation, the single-particle operator of the bosonic atoms can be written as [1]

$$b_j^{\dagger} = (a\rho)^{\frac{1}{2}} \left\{ e^{-i\theta(a_j)} + \sum_{p \neq 0} e^{i2p[\pi\rho a_j - \phi(a_j)]} e^{-i\theta(a_j)} \right\}, \quad (7)$$

with ρ the density and a the lattice spacing. In the following, we take $a = 1$.

B. Matrix product state ground-state simulations

The numerical results were obtained using a finite-size DMRG algorithm in the matrix product state (MPS) representation [56–60], implemented using the ITENSOR library [61]. We compute the ground state of model (1) for ladders with a number of rungs between $L = 60$ and $L = 180$, and with a maximal bond dimension up to 1800. This ensures that the truncation error is at most 10^{-9} . Since we are considering a bosonic model with finite interactions the local Hilbert space

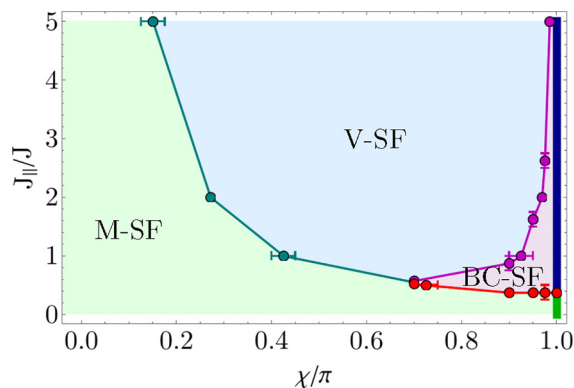


FIG. 3. Sketch of the phase diagram for half filling, $\rho = 0.5$, for $U/J = 2.5$. The identified phases (see text) are the Meissner superfluid (M-SF), the vortex superfluid (V-SF), and the biased chiral superfluid (BC-SF). At $\chi = \pi$ (marked by a thick vertical line) we have a phase transition between a superfluid (green) and a chiral superfluid (dark blue).

is very large; thus, a cutoff for its dimension is needed. We use a maximal local dimension of at least four or five bosons per site. We checked that the local states with a higher number of bosons per site do not have an occupation larger than 10^{-5} for the parameters considered. We make use of good quantum numbers in our implementation as the number of atoms is conserved in the considered model.

IV. PHASE DIAGRAM AT HALF FILLING, $\rho = 0.5$

In this section, we focus for the case in which we have one bosonic atom every two sites, $\rho = 0.5$. In Fig. 3 we sketch the phase diagram we obtain from our numerical and analytical results which we detail in the following. In particular, we focus on several regions on the phase diagram. We investigate the limit of small J_{\parallel} (see Sec. IV A), where we obtain a Meissner superfluid (M-SF). At large J_{\parallel} we observe a phase transition between the M-SF and a vortex superfluid (V-SF) state (see Sec. IV B). At $\chi = \pi$ a transition between a superfluid and a chiral superfluid state is present (Sec. IV C), and for $\chi \lesssim \pi$ the chiral superfluid extends to a biased chiral superfluid phase (BC-SF) phase. Throughout this section the value of the on-site interaction is $U/J = 2.5$.

A. Small- J_{\parallel} limit, single-chain limit

In the regime of small J_{\parallel}/J it is useful to rewrite the Hamiltonian given in Eq. (1) as a single chain with long-range complex hopping:

$$H_{\text{chain}} = -J_{\parallel} \sum_j [e^{i(-1)^j \chi} b_j^{\dagger} b_{j+2} + \text{H.c.}]$$

$$- J \sum_j (b_j^{\dagger} b_{j+1} + \text{H.c.})$$

$$+ \frac{U}{2} \sum_j n_j (n_j - 1). \quad (8)$$

In this case the bosonized Hamiltonian is

$$H_{\text{chain}} = \int \frac{dx}{2\pi} \{ [uK + 16\pi\rho J_{\parallel} \cos(\chi)] \partial_x \theta(x)^2 + \frac{u}{K} \partial_x \phi(x)^2 \} + \rho^2 U \int dx \cos[2p\phi(x)], \quad (9)$$

with the velocity u , Luttinger parameter K , and $p = 1$ for $\rho = 1$ and $p = 2$ for $\rho = 0.5$. For the atomic density considered in this section we expect that the interaction term does not dominate and we obtain a Luttinger liquid for which the Luttinger parameter depends on the flux χ . As we see in the following this is in agreement with our numerical results. However, we note slight deviations from the analytical expectation of the dependence of effective Luttinger parameter on χ and the numerical results (see Appendix B).

In the single-chain limit the local current observables (4) can be rewritten as

$$\begin{aligned} j_j^{\perp} &= -iJ(b_j^{\dagger}b_{j+1} - \text{H.c.}), \\ j_j^{\parallel} &= -iJ_{\parallel}[e^{(-1)^j i\chi} b_j^{\dagger}b_{j+2} - \text{H.c.}]. \end{aligned} \quad (10)$$

In terms of the bosonic field the currents read

$$\begin{aligned} j_j^{\perp} &= 2\rho J \sin(\partial_x \theta), \\ j_j^{\parallel} &= 2\rho J_{\parallel} \sin \left[2 \left(\partial_x \theta + (-1)^j \frac{\chi}{2} \right) \right], \\ j_{j+1}^{\parallel} - j_j^{\parallel} &= 2\rho J_{\parallel} \cos(2\partial_x \theta) \sin(\chi). \end{aligned} \quad (11)$$

In the obtained gapless phase the expectation value of the rung currents will average to zero, and the chiral current has a finite value $J_c \propto \sum_j (j_{j,1}^{\parallel} - j_{j,2}^{\parallel}) \propto \sin(\chi)$. These results are consistent with the currents expected in the Meissner superfluid phase, which are depicted in Fig. 4(a), and their values are shown in Fig. 5.

In Fig. 5 at small values of the leg tunneling amplitude, $J_{\parallel}/J = 0.2$, we observe that the currents on the rungs are close to zero and the chiral current, J_c , has a finite value stable with increasing the system size. The central charge is $c \approx 1$ for all values of the flux, implying the existence of one gapless mode. Furthermore, in this phase, the single-particle correlations decay algebraically with the distance (see Appendix B). Based on these considerations we can identify the Meissner superfluid state. However, we identify some small deviations from the expected $\sin(\chi)$ dependence of the chiral current (Fig. 5).

We can observe in Eq. (9) for large values of J_{\parallel} and $\chi \approx \pi$ the coefficient of the first term in the Hamiltonian will vanish and eventually become negative. This instability in our bosonized model could signal a phase transition. In the numerical results for $J_{\parallel}/J = 0.5$, presented in Fig. 6, we see above $\chi \gtrsim 0.75$ a phase with strong currents and central charge $c \approx 1$. Furthermore, a finite density imbalance between the two legs of the ladder is present. We associate this regime with the biased chiral superfluid phase. We describe in more details the nature of this phase in Sec. IV D.

We observe in the numerical results that the value of the Luttinger parameter extracted from the algebraic decay of the single-particle correlations decreases and it is close to zero as we increase χ towards the phase transition between

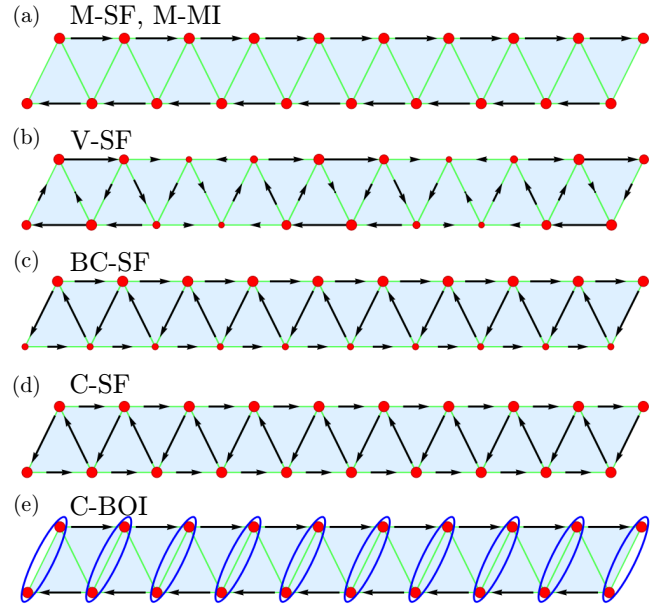


FIG. 4. The pattern of currents, depicted with arrows, and local densities, depicted with red disks, obtained in the numerical ground-state results for the (a) Meissner states (M-SF, or M-MI), (b) vortex superfluid phases (V-SF), (c) biased chiral superfluid (BC-SF), (d) chiral superfluid (C-SF), and (e) chiral bond order insulator (C-BOI), where we also marked the bond ordering on every second rung. We note that the local currents are not normalized to the same value for the different phases represented in the four sketches.

the Meissner superfluid and the biased chiral superfluid (see Appendix B).

B. Large- J_{\parallel} limit, two-coupled-chains limit

We bosonize the Hamiltonian of the two coupled chains (1) in the limit where tunneling J_{\parallel} along the two chains dominates. In this regime we have a pair of bosonic fields for each

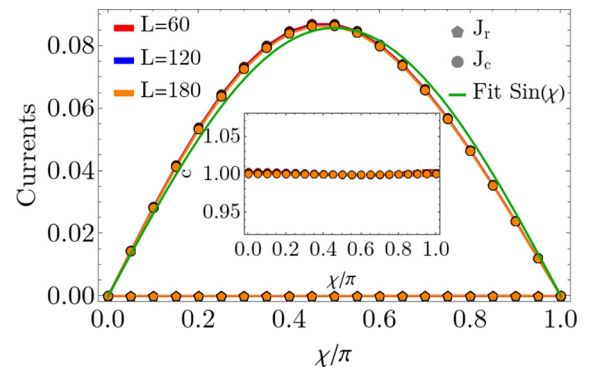


FIG. 5. Numerical ground-state results for the average rung current, J_r , and the chiral current, J_c , as a function of the flux χ for $J_{\parallel}/J = 0.2$, $U/J = 2.5$, $\rho = 0.5$, and $L \in \{60, 120, 180\}$. The inset contains the dependence of the central charge, c , on the flux. We can identify the Meissner superfluid phase. We note that the markers corresponding to the smaller system sizes are below the ones for $L = 180$. The maximal bond dimension used was $m = 500$ for $L = 60$, $m = 900$ for $L = 120$, and $m = 1500$ for $L = 180$.

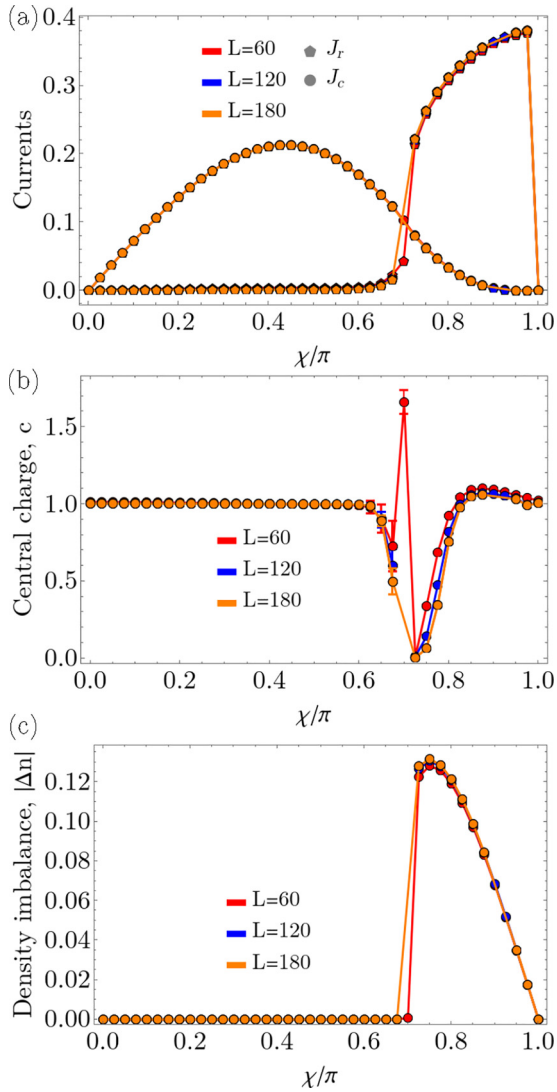


FIG. 6. Numerical ground-state results for (a) the average rung current, J_r , and the chiral current, J_c , (b) the central charge, c , and (c) the absolute value of the density imbalance, $|\Delta n|$, as a function of the flux χ for $J_{\parallel}/J = 0.5$, $U/J = 2.5$, $\rho = 0.5$, and $L \in \{60, 120, 180\}$. We observe a transition from the Meissner superfluid to the biased chiral superfluid at $\chi \approx 0.75\pi$. The maximal bond dimension used was $m = 600$ for $L = 60$, $m = 1200$ for $L = 120$, and $m = 1800$ for $L = 180$.

leg of the ladder:

$$\begin{aligned}
 H_{2\text{chains}} = & \int \frac{dx}{2\pi} \left\{ uK[\partial_x \theta_1(x) - \chi]^2 + \frac{u}{K} \partial_x \phi_1(x)^2 \right\} \\
 & + \int \frac{dx}{2\pi} \left\{ uK[\partial_x \theta_2(x) + \chi]^2 + \frac{u}{K} \partial_x \phi_2(x)^2 \right\} \\
 & + \rho^2 U \sum_m \int dx \cos[2p\phi_m(x)] \\
 & - 4\rho J \int dx \cos[\theta_1(x) - \theta_2(x)]. \quad (12)
 \end{aligned}$$

In the following, we rewrite the Hamiltonian in terms of the symmetric and antisymmetric combinations of the bosonic

fields, $\phi_{s(a)} = \frac{1}{\sqrt{2}}(\phi_1 \pm \phi_2)$ and $\theta_{s(a)} = \frac{1}{\sqrt{2}}(\theta_1 \pm \theta_2)$:

$$\begin{aligned}
 H_{2\text{chains}} = & \int \frac{dx}{2\pi} \left[uK \partial_x \theta_s(x)^2 + \frac{u}{K} \partial_x \phi_s(x)^2 \right] \\
 & + \int \frac{dx}{2\pi} \left\{ uK[\partial_x \theta_a(x) - \sqrt{2}\chi]^2 + \frac{u}{K} \partial_x \phi_a(x)^2 \right\} \\
 & + \rho^2 U \int dx \cos[\sqrt{2}p\phi_s(x)] \cos[\sqrt{2}p\phi_a(x)] \\
 & - 4\rho J \int dx \cos[\sqrt{2}\theta_a(x)]. \quad (13)
 \end{aligned}$$

Similarly the local currents (3) can be written as

$$\begin{aligned}
 j_j^{\perp} &= 2\rho J \sin(\sqrt{2}\theta_a), \\
 j_{j,1}^{\parallel} - j_{j,2}^{\parallel} &= 2\rho J_{\parallel} \cos\left(\frac{1}{\sqrt{2}}\partial_x \theta_s\right) \sin\left(\frac{1}{\sqrt{2}}\partial_x \theta_a - \chi\right). \quad (14)
 \end{aligned}$$

In the case of half filling, $\rho = N/(2L) = 0.5$, considered in this section, we do not have commensurability effects induced by the interaction term [third line in Eq. (13)]. We can observe in the sketch of the phase diagram, Fig. 3, that at $J_{\parallel}/J = 2$ and $\chi \approx 0.25\pi$ we have a transition between the Meissner superfluid and a vortex superfluid phase. This phase transition can be understood by analyzing the relevance of the term $J \cos[\sqrt{2}\theta_a(x)]$ in Hamiltonian (13). We note that we describe the nature of the biased chiral superfluid phase occurring for small $\pi - \chi$ separately in Sec. IV D.

When the term $J \cos[\sqrt{2}\theta_a(x)]$ dominates, we have a gapless symmetric mode and a gapped antisymmetric mode for which the field is pinned to the minima of the potential, $\theta_a = 0$. In this case the rung currents vanish and the chiral current $J_c \propto \sin(\chi)$; thus, this corresponds to the Meissner superfluid. This is in agreement with the numerical results presented in Fig. 7(a) for the low values of χ . The central charge in this regime is $c = 1$, as seen in Fig. 7(c).

If both the symmetric and antisymmetric sectors are gapless we have the vortex superfluid. The vortex phase exhibits incommensurate currents patterns, as, for example, depicted in Fig. 4(b). One can identify this phase for $0.25 \lesssim \chi \lesssim 0.95$, as seen from the values of the average of the rung and chiral currents in Fig. 7(a). We extract numerically the vortex density by performing the Fourier transform of the space dependence of the rung currents and obtaining the periodicity of the vortices. The vortex density is plotted in Fig. 7(b) as a function of the flux, which shows a linear behavior. This dependence can be understood in bosonization by computing the rung current-current correlations

$$\begin{aligned}
 \langle j^{\perp}(x) j^{\perp}(0) \rangle &= 4\rho^2 J^2 \langle \sin[\sqrt{2}\theta_a(x)] \sin[\sqrt{2}\theta_a(0)] \rangle \\
 &= 2\rho^2 J^2 \langle \cos[\sqrt{2}(\theta_a(x) - \theta_a(0))] \rangle \\
 &\propto x^{-1/(4K)} \cos(\chi x), \quad (15)
 \end{aligned}$$

where x is the lattice position in the continuum limit. The frequency of the oscillations gives the expected vortex density, in agreement with the values obtained numerically in Fig. 7(b). We note that we do not observe any commensurate vortex densities ρ_v , as obtained for the square ladder [3].

We can observe that the finite-size effects are more prominent in the vortex phase, both in the currents [Fig. 7(a)] and

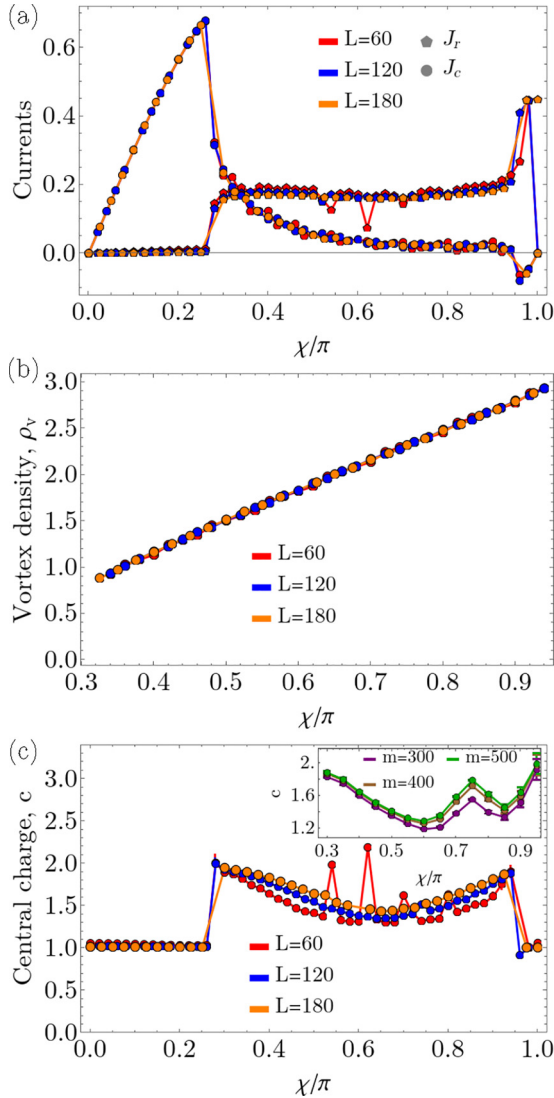


FIG. 7. Numerical ground-state results for (a) the average rung current, J_r , and the chiral current, J_c , (b) vortex density, ρ_v , and (c) the central charge, c , as a function of the flux χ for $J_{\parallel}/J = 2$, $U/J = 2.5$, $\rho = 0.5$, and $L \in \{60, 120, \dots\}$. We observe a transition from the Meissner superfluid to the vortex superfluid around $\chi \approx 0.27\pi$ and a transition to biased chiral superfluid at $\chi \approx 0.95\pi$. The maximal bond dimension used was $m = 600$ for $L = 60$, $m = 1100$ for $L = 120$, and $m = 1800$ for $L = 180$. In the inset of (c) we plot the central charge in the vortex superfluid regime for $L = 60$ and different bond dimensions $m \in \{300, 400, 500\}$.

the central charge [Fig. 7(c)]. However, as we increase the system size the value of the central charge becomes closer to the expected value of $c = 2$; similarly in the inset of Fig. 7(c) we analyze the impact of the numerical bond dimension used in the MPS representation. The behavior of the system for χ close to and equal to π is discussed in the following sections.

C. Fully frustrated ladder at $\chi = \pi$

In the following, we analyze the behavior in the case of $\chi = \pi$. In the phase diagram this corresponds to a particular

line, marked in Fig. 3. In this case Hamiltonian (1) becomes

$$\begin{aligned}
 H = & J_{\parallel} \sum_j (b_{j,1}^{\dagger} b_{j+1,1} + b_{j,2}^{\dagger} b_{j+1,2} + \text{H.c.}) \\
 & - J \sum_j (b_{j,1}^{\dagger} b_{j,2} + b_{j+1,1}^{\dagger} b_{j,2} + \text{H.c.}) \\
 & + \frac{U}{2} \sum_j n_{j,m} (n_{j,m} - 1).
 \end{aligned} \quad (16)$$

We employ the transformation $b_{j,m} \rightarrow (-1)^j b_{j,m}$ to change the sign of the kinetic energy along the legs and obtain

$$\begin{aligned}
 H = & -J_{\parallel} \sum_j (b_{j,1}^{\dagger} b_{j+1,1} + b_{j,2}^{\dagger} b_{j+1,2} + \text{H.c.}) \\
 & - J \sum_j (b_{j,1}^{\dagger} b_{j,2} - b_{j+1,1}^{\dagger} b_{j,2} + \text{H.c.}) \\
 & + \frac{U}{2} \sum_j n_{j,m} (n_{j,m} - 1).
 \end{aligned} \quad (17)$$

In this representation, the hopping on the rungs has an alternating sign. Similar models have been investigated in Refs. [36,62]. The alternating rung-hopping terms cancel the lowest-order term which we considered in the previous sections, such that we have to take into account the next-order terms of the expansion in the bosonic fields,

$$\begin{aligned}
 b_{j,1}^{\dagger} b_{j,2} &= \rho e^{-i[\theta_1(a_j) - \theta_2(a_j) - \frac{\alpha}{2} \partial_x \theta_2(a_j)]}, \\
 b_{j+1,1}^{\dagger} b_{j,2} &= \rho e^{-i[\theta_1(a_j) - \theta_2(a_j) + \frac{\alpha}{2} \partial_x \theta_1(a_j)]},
 \end{aligned} \quad (18)$$

where the gradients stem from the triangular geometry of the ladder. We obtain for the tunneling along the rungs

$$\begin{aligned}
 H_{\perp} = & -2\rho J \int dx \left\{ \cos \left[\theta_1(x) - \theta_2(x) - \frac{1}{2} \partial_x \theta_2(x) \right] \right. \\
 & \left. - \cos \left[\theta_1(x) - \theta_2(x) + \frac{1}{2} \partial_x \theta_1(x) \right] \right\} \\
 = & -2\rho J \int dx \sin \left(\sqrt{2} \theta_a + \frac{1}{\sqrt{2}} \partial_x \theta_a \right) \sin \left(\frac{1}{\sqrt{2}} \partial_x \theta_s \right) \\
 \approx & -\sqrt{2} \rho J \int dx \sin(\sqrt{2} \theta_a) \partial_x \theta_s,
 \end{aligned} \quad (19)$$

where in the last line we expanded the sine and neglected the contributions stemming from $\partial_x \theta_a$. In the regime H_{\perp} dominates, one obtains ground states which break the \mathbb{Z}_2 symmetry of the model, for example, obtaining a spin nematic phase in a triangular spin ladder [63], or a chiral superfluid in a bosonic zigzag ladder [62].

The coupling between θ_s and θ_a present in H_{\perp} can be analyzed with the help of a self-consistent mean-field approach [63]. We outline this approach in Appendix C. We obtain two solutions for the ground state, which break the \mathbb{Z}_2 symmetry, for which the field θ_a is fixed either to $\frac{\pi}{2\sqrt{2}}$, or to $\frac{3\pi}{2\sqrt{2}}$, and for both $\langle \partial_x \theta_s(x) \rangle$ has a finite value.

Using the results of the mean-field theory, we can compute the currents present in the triangular ladder:

$$\begin{aligned}
j_j^\perp &= -iJ(b_{j,1}^\dagger b_{j,2} - \text{H.c.}) \\
&\propto \sin(\sqrt{2}\theta_a) \cos\left(\frac{1}{4}\partial_x\theta_s\right), \\
j_j^\perp + j_{j+1}^\perp &= -iJ(b_{j,1}^\dagger b_{j,2} - b_{j+1,1}^\dagger b_{j,2} - \text{H.c.}) \\
&\propto \cos(\sqrt{2}\theta_a) \sin\left(\frac{1}{\sqrt{2}}\partial_x\theta_s\right) = 0, \quad (20) \\
j_{j,1}^\parallel &= -iJ_\parallel(b_{j,1}^\dagger b_{j+1,1} - \text{H.c.}) \\
&\propto \sin\left(\frac{1}{\sqrt{2}}\partial_x\theta_s\right) \cos\left(\frac{1}{\sqrt{2}}\partial_x\theta_a\right) \\
&\quad + \cos\left(\frac{1}{\sqrt{2}}\partial_x\theta_s\right) \sin\left(\frac{1}{\sqrt{2}}\partial_x\theta_a\right) \propto \partial_x\theta_s, \\
j_{j,2}^\parallel &= -iJ_\parallel(b_{j,2}^\dagger b_{j+1,2} - \text{H.c.}) \\
&\propto \partial_x\theta_s, \\
j_{j,1}^\parallel - j_{j,2}^\parallel &\propto \cos\left(\frac{1}{\sqrt{2}}\partial_x\theta_s\right) \sin\left(\frac{1}{\sqrt{2}}\partial_x\theta_a\right) = 0. \quad (21)
\end{aligned}$$

We have obtained the chiral superfluid (C-SF) phase [62], in which we have finite currents on the rungs, equal but with opposite directions on consecutive rungs, and finite currents on the legs flowing in the same direction on the two legs. The pattern is depicted in Fig. 4(d). The direction of the currents is determined by which of the two \mathbb{Z}_2 -symmetry-broken states one considers.

Thus, for $\chi = \pi$ at half filling we expect to observe a superfluid phase at small values of J_\parallel/J (depicted with the thick green line for $\chi = \pi$ in Fig. 3), and the chiral superfluid phase (depicted with the thick dark blue line for $\chi = \pi$ in Fig. 3). This is in agreement with the numerical ground-state results, shown in Fig. 8.

The central charge varies only slightly as a function of J_\parallel around the expected value for the two phases, $c = 1$ [see Fig. 8(a)]. If we look at the average rung current we find that they are vanishing both in Fig. 6(a) for $J_\parallel/J = 0.5$ and in Fig. 7(a) for $J_\parallel/J = 2$. However, this does not imply that we cannot be in the chiral superfluid phase for these parameters. One explanation can be that in our numerical ground-state calculations we converge to an equal superposition of the two possible \mathbb{Z}_2 -symmetry-broken states (Appendix C). This would imply that the measured expectation values of the measured local currents are zero, as the currents in the two states have the same magnitude, but a different sign. In order to confirm this behavior we compute the following rung-rung correlations:

$$\begin{aligned}
c_+(d) &= (b_{j,1}^\dagger b_{j,2} + b_{j,2}^\dagger b_{j,1})(b_{j+d,2}^\dagger b_{j+d,1} + b_{j+d,1}^\dagger b_{j+d,2}) \\
&\propto \cos[\sqrt{2}\theta_a(x=ad)] \cos[\sqrt{2}\theta_a(0)], \\
c_-(d) &= (b_{j,1}^\dagger b_{j,2} - b_{j,2}^\dagger b_{j,1})(b_{j+d,2}^\dagger b_{j+d,1} - b_{j+d,1}^\dagger b_{j+d,2}) \\
&\propto \sin[\sqrt{2}\theta_a(x=ad)] \sin[\sqrt{2}\theta_a(0)]. \quad (22)
\end{aligned}$$

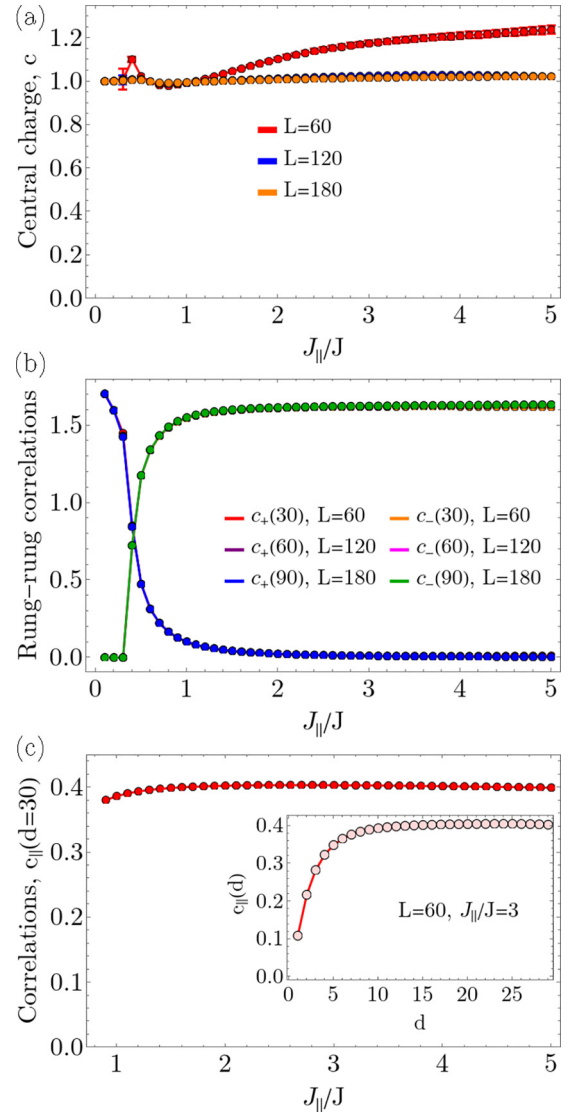


FIG. 8. Numerical ground-state results for (a) the central charge, (b) the saturation value of the rung-rung correlations c_\pm [Eqs. (22)], and (c) the saturation value of the current-current correlations on the legs c_\parallel [Eq. (23)], as a function of J_\parallel , for $\chi = \pi$, $U/J = 2.5$, $\rho = 0.5$, and $L \in \{60, 120, 180\}$. In the inset of (c) we show the distance dependence of $c_\parallel(d)$ at $J_\parallel/J = 3$. We observe a transition from the superfluid to the chiral superfluid at $J_\parallel/J \approx 0.35$. The maximal bond dimension used was $m = 500$ for $L = 60$, $m = 1000$ for $L = 120$, and $m = 1500$ for $L = 180$.

In Fig. 8(b) one can observe that for $J_\parallel/J \lesssim 0.3$ we find that c_+ saturates at long distances ($d = 30$), signaling that θ_a orders in the potential of the $\cos(\sqrt{2}\theta_a)$ term. This phase corresponds to a superfluid state as the $\chi \rightarrow \pi$ limit of the Meissner superfluid. When we increase $J_\parallel/J \gtrsim 0.3$ we see that c_+ decreases to a small value at the longest distance we consider and c_- is the one that saturates at large distances, implying that $\sin(\sqrt{2}\theta_a)$ gaps the antisymmetric sector, as expected for the chiral superfluid phase. This is further supported by the current-current correlations along the legs:

$$\begin{aligned}
c_\parallel(d) &= J_\parallel^2 (b_{j,m}^\dagger b_{j+1,m} - b_{j+1,m}^\dagger b_{j,m}) \\
&\quad \times (b_{j+d,m}^\dagger b_{j+d+1,m} - b_{j+d+1,m}^\dagger b_{j+d,m}). \quad (23)
\end{aligned}$$

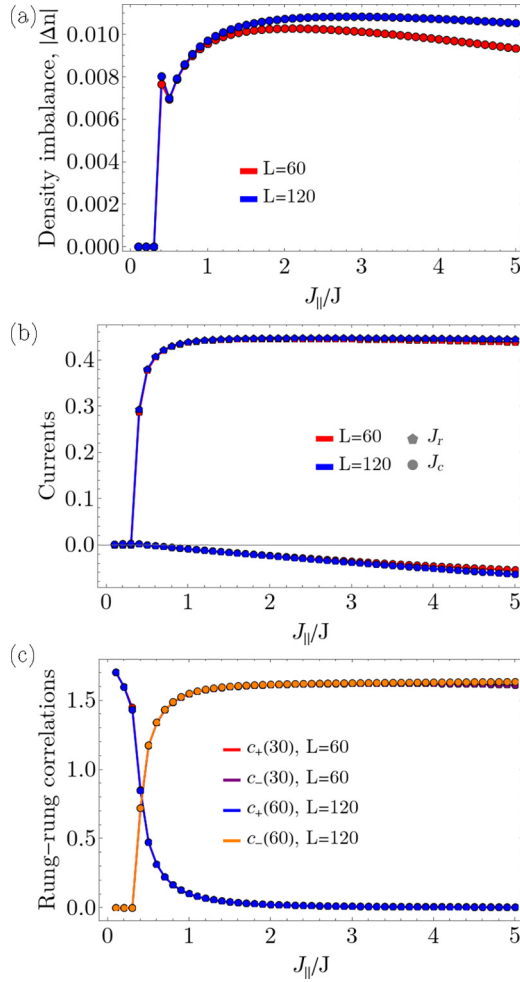


FIG. 9. Numerical ground-state results for (a) the absolute value of the density imbalance, $|\Delta n|$, (b) the average rung current, J_r , and the chiral current, J_c , and (c) the saturation value of the rung-rung correlations c_{\pm} [Eqs. (22)], as a function of J_{\parallel} , for $\chi = 0.99\pi$, $U/J = 2.5$, $\rho = 0.5$, and $L \in \{60, 120\}$. We observe a transition from the Meissner superfluid to the biased chiral superfluid at $J_{\parallel}/J \approx 0.35$. The maximal bond dimension used was $m = 600$ for $L = 60$ and $m = 1200$ for $L = 120$. We note that the apparent nonmonotonic behavior seen in $|\Delta n|$ in (a) for $J_{\parallel}/J \approx 0.4$ is within the numerical errors in the regime close to the phase transition and it is not observed in the observables depicted in (b) and (c).

In order to reduce the finite-size effects in the numerical calculation of $c_+(d)$, $c_-(d)$, and $c_{\parallel}(d)$ [Eqs. (22) and (23)] [presented in Figs. 8(b) and 8(c), Figs. 10(b) and 10(c), and Fig. 9] we normalized $b_{j,m} \rightarrow b_{j,m}/\sqrt{\langle n_{j,m} \rangle}$. The leg current-current correlations, Fig. 8(c), are finite in the regime corresponding to the chiral superfluid and almost constant as a function of J_{\parallel} . In the inset of Fig. 8(c) we show the saturation behavior of the current-current correlations at large distances.

We note that, depending on the initial states and gauge chosen in the numerical calculations, one can converge to just one of the \mathbb{Z}_2 -symmetry-broken states and see finite values of the currents as presented in Fig. 4(d). We give more details in this regard in Appendix D.

D. Large- J_{\parallel} limit and small $\chi_0 = \pi - \chi$

In this section, we address the question if the chiral superfluid phase extends also at finite values of $\chi_0 = \pi - \chi$, as we can observe for $J_{\parallel}/J = 2$ in Fig. 7(c) a transition to a $c = 1$ phase above $\chi \approx 0.95\pi$. We approach this by rewriting Hamiltonian (1) in terms of χ_0 :

$$\begin{aligned}
 H = & J_{\parallel} \sum_j (e^{i\chi_0} b_{j,1}^{\dagger} b_{j+1,1} + e^{-i\chi_0} b_{j,2}^{\dagger} b_{j+1,2} + \text{H.c.}) \\
 & - J \sum_j (b_{j,1}^{\dagger} b_{j,2} + b_{j+1,1}^{\dagger} b_{j,2} + \text{H.c.}) \\
 & + \frac{U}{2} \sum_j n_{j,m} (n_{j,m} - 1). \quad (24)
 \end{aligned}$$

Employing the transformation $b_{j,m} \rightarrow (-1)^j b_{j,m}$, as in Sec. IV C we obtain

$$\begin{aligned}
 H = & -J_{\parallel} \sum_j (e^{i\chi_0} b_{j,1}^{\dagger} b_{j+1,1} + e^{-i\chi_0} b_{j,2}^{\dagger} b_{j+1,2} + \text{H.c.}) \\
 & - J \sum_j (b_{j,1}^{\dagger} b_{j,2} - b_{j+1,1}^{\dagger} b_{j,2} + \text{H.c.}) \\
 & + \frac{U}{2} \sum_j n_{j,m} (n_{j,m} - 1). \quad (25)
 \end{aligned}$$

The bosonized Hamiltonian, in terms of the symmetric and antisymmetric fields, is given by

$$\begin{aligned}
 H = & \int \frac{dx}{2\pi} \left[uK \partial_x \theta_s(x)^2 + \frac{u}{K} \partial_x \phi_s(x)^2 \right] \\
 & + \int \frac{dx}{2\pi} \left\{ uK [\partial_x \theta_a(x) + \sqrt{2} \chi_0/a]^2 + \frac{u}{K} \partial_x \phi_a(x)^2 \right\} \\
 & + \rho^2 U \int dx \cos[\sqrt{2} p \phi_s(x)] \cos[\sqrt{2} p \phi_a(x)] \\
 & - \sqrt{2} \rho J \int dx \sin[\sqrt{2} \theta_a(x)] \partial_x \theta_s(x). \quad (26)
 \end{aligned}$$

We observe that the Hamiltonian is similar to the one obtained in Eq. (13) for the two coupled chains. However, it exhibits the same coupling between the symmetric and antisymmetric sectors as in the case of $\chi = \pi$ [Eq. (19)]. Thus, when both sectors are gapless one would obtain the vortex superfluid phase. In the following, we analyze the case in which the coupling $\sin[\sqrt{2} \theta_a(x)] \partial_x \theta_s(x)$ gaps the antisymmetric sector, by looking at the behavior of the currents:

$$\begin{aligned}
 j_j^{\perp} &= -iJ(b_{j,1}^{\dagger} b_{j,2} - \text{H.c.}) \propto \sin(\sqrt{2} \theta_a), \\
 j_j^{\perp} + j_{j+1}^{\perp} &= -iJ(b_{j,1}^{\dagger} b_{j,2} - b_{j+1,1}^{\dagger} b_{j,2} - \text{H.c.}) \\
 &\propto \cos(\sqrt{2} \theta_a) \sin\left(\frac{1}{\sqrt{2}} \partial_x \theta_s\right) = 0, \\
 j_{j,1}^{\parallel} - j_{j,2}^{\parallel} &= -2\rho J_{\parallel} \cos\left(\frac{1}{\sqrt{2}} \partial_x \theta_s\right) \sin\left(\frac{1}{\sqrt{2}} \partial_x \theta_a + \chi_0\right) \\
 &\propto \sin(\chi_0) = \sin(\chi). \quad (27)
 \end{aligned}$$

In this situation, we obtain two degenerate ground states breaking the \mathbb{Z}_2 symmetry of the ladder, with a similar pattern of currents as in the case of $\chi = \pi$ for the chiral superfluid

[Eqs. (20) and (21)]. However, at finite χ_0 the currents on the legs have different values, even though they flow in the same direction. The pattern of the currents is depicted in Fig. 4(c). As the currents on the two consecutive rungs are equal, this implies that the densities on the two legs of the ladder have to be different, due to the continuity relation between densities and currents. Thus, there exists a density imbalance between the two legs of the ladder. We label this phase as the biased chiral superfluid. We note that the biased chiral superfluid phase is not the direct equivalent of the biased ladder phase observed in square ladders [12,19], as in the biased phase of the square ladder the currents resemble the ones in the Meissner phase. In the considered model, due to the geometry of the triangular ladder, we obtain a biased phase with similar currents as in the chiral superfluid.

Numerically, we analyze the case of $\chi = 0.99\pi$ as a function of the value of J_{\parallel}/J , Fig. 9. Above $J_{\parallel}/J \approx 0.35$ we observe that the density imbalance becomes finite [see Fig. 9(a)]. This fact together with the finite currents, Fig. 9(b), points towards the biased chiral superfluid. The behavior of the rung-rung correlations shown in Fig. 9(c) is very similar to the one observed for $\chi = \pi$ in Fig. 8. The computed observables have a weak dependence as we increase J_{\parallel}/J above the transition threshold; thus, we can be confident that the imbalanced phase observed at small values of J_{\parallel} in Sec. IV A has the same nature as at large J_{\parallel} . We discuss the numerical challenges in converging in the degenerate ground-state manifold in Appendix D.

E. Transition to the square ladder

An interesting extension of the model for the triangular ladder at $\chi = \pi$ [Eq. (17)] is the interpolation towards the square ladder without a flux, as in the following:

$$\begin{aligned}
 H = & -J_{\parallel} \sum_j (b_{j,1}^{\dagger} b_{j+1,1} + b_{j,2}^{\dagger} b_{j+1,2} + \text{H.c.}) \\
 & - J \sum_j (b_{j,1}^{\dagger} b_{j,2} + \text{H.c.}) \\
 & + (J - t) \sum_j (b_{j+1,1}^{\dagger} b_{j,2} + \text{H.c.}) \\
 & + \frac{U}{2} \sum_j n_{j,m} (n_{j,m} - 1), \quad (28)
 \end{aligned}$$

for $t = 0$ we recover Eq. (17) and for $t = J$ we obtain a square ladder.

In the bosonized language we obtain for the tunneling along the rungs

$$\begin{aligned}
 H_{\perp} = & -\sqrt{2}\rho J \int dx \sin(\sqrt{2}\theta_a) \partial_x \theta_s \\
 & - 2\rho t \int dx \cos(\sqrt{2}\theta_a). \quad (29)
 \end{aligned}$$

This model allows us to investigate the existence of the mean-field solutions in the case in which the field θ_a is not pinned in the minima of the potential $\sin(\sqrt{2}\theta_a)$, but at a different value due to the presence of the additional term $\cos(\sqrt{2}\theta_a)$.

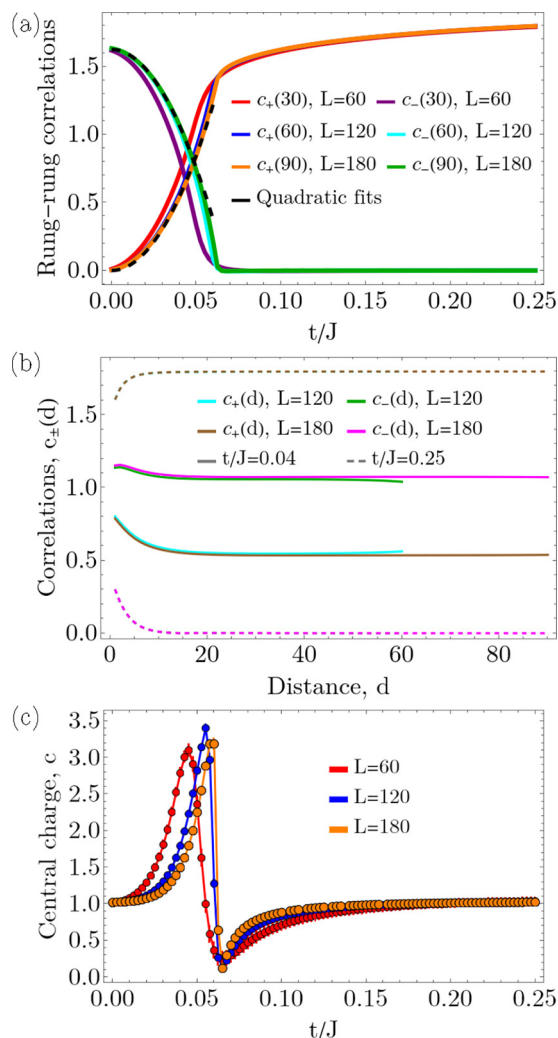


FIG. 10. Numerical ground-state results for (a) the saturation value of the rung-rung correlations c_{\pm} [Eqs. (22)] as a function of the parameter t interpolating between the triangular ladder at $\chi = \pi$ and the square ladder without a flux. The black lines depict the fit of the dependence on t as given in Eq. (30). (b) The decay of the rung-rung correlations c_{\pm} as a function of distance for $t/J \in \{0.04, 0.25\}$ and $L \in \{120, 180\}$. Note that the continuous lines correspond to $t/J = 0.04$ and the dashed lines to $t/J = 0.25$. (c) The central charge, c , as a function of t/J . The parameters used are $J_{\parallel}/J = 5$, $U/J = 2.5$, $\rho = 0.5$, and $L \in \{60, 120, 180\}$. The maximal bond dimension used was $m = 500$ for $L = 60$, $m = 1000$ for $L = 120$, and $m = 1500$ for $L = 180$.

We show how one can perform the mean-field approach for this situation in Appendix C.

In the case of $t = 0$ we saw in the previous section that at the large value of J_{\parallel}/J the field θ_a is pinned to the minima of the potential $\pm \sin(\sqrt{2}\theta_a)$. In the limit of $t/J \rightarrow 1$, as we get closer to the square ladder, the field θ_a will be pinned to the minima of the potential $\cos(\sqrt{2}\theta_a)$. However, in between these two values we can expect a chiral superfluid regime in which $\langle \theta_a \rangle$ corresponds to the minima of the sum of the two potentials, as described in Appendix C, and a transition to a superfluid state for which the field is pinned to $\theta_a = 0$. Based on the mean-field approach we can analyze the behavior of the

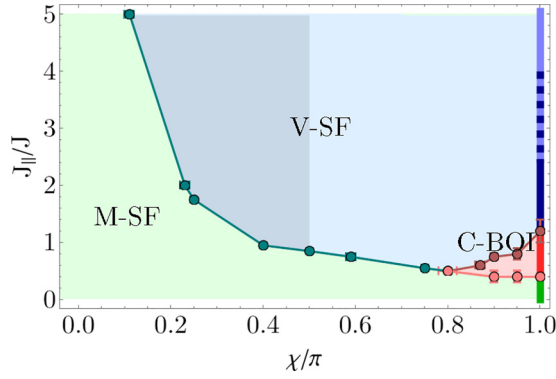


FIG. 11. Sketch of the phase diagram for hard-core bosons at half filling, $\rho = 0.5$, $U/J = \infty$. The identified phases (see text) are the Meissner superfluid (M-SF), the vortex superfluid (V-SF), and chiral bond order insulator (C-BOI). In the shaded area in the vortex phase, which extends up to $\chi = 0.5\pi$, we identified also a commensurate frequency in the behavior of the currents. At $\chi = \pi$ (marked by a thick vertical line) we observe the following phases: a superfluid phase (green), a bond order insulator (red), a chiral superfluid phase (dark blue), and a two-mode superfluid (blue). The phase transition between the chiral superfluid and the two-mode superfluid shows large finite-size effects in the dashed region [see the explanation in the main text, Fig. 14(b), and Appendix D].

saturation value of the correlations c_- and c_+ as a function of t (see Appendix C),

$$\begin{aligned} c_-(d \rightarrow \infty) &\propto a_- - b_- t^2, \\ c_+(d \rightarrow \infty) &\propto b_+ t^2, \end{aligned} \quad (30)$$

where a_- , b_- , and b_+ are constant, which can depend on the other parameters of the model. In Fig. 10(a) we observe that for $t \lesssim 0.07$ the scaling of the saturation value of the correlations c_- and c_+ as a function of t is in agreement with the results of the mean-field theory [Eqs. (30)]. This shows that the value of $\langle \theta_a \rangle$ depends on the value of t . Above $t \gtrsim 0.07$, only c_+ saturates to a finite value at large distances which means that the term $\cos(\sqrt{2}\theta_a)$ dominates and $\langle \theta_a \rangle = 0$. The saturation behavior of the correlations c_{\pm} as a function of distance in the two regimes is shown in Fig. 10(b). The central charge, Fig. 10(c), has values $c \approx 1$ in both phases and strong variation close to the phase transition. However, the region in which it deviates from the expected $c = 1$ value becomes smaller for the larger system sizes.

V. PHASE DIAGRAM OF HARD-CORE BOSONS, $\rho = 0.5$

In this section, we analyze the phase diagram in the case of hard-core bosons at half filling, $\rho = N/(2L) = 0.5$.

For $\chi < 0.8\pi$, we obtain a phase diagram (see Fig. 11) similar for the finite interaction half-filling case (Sec. IV), in which we observe a phase transition between a Meissner superfluid and a vortex superfluid. The behavior of the chiral and rung currents is shown in Figs. 12(a) and 12(b), for $J_{||}/J = 2$. In Fig. 12(c) we see the jump from $c \approx 1$ to $c \approx 2$ in the central charge signaling the phase transition. However, even though in the vortex phase we obtain finite values for the average rung current and chiral current for $\chi > 0.5\pi$, the

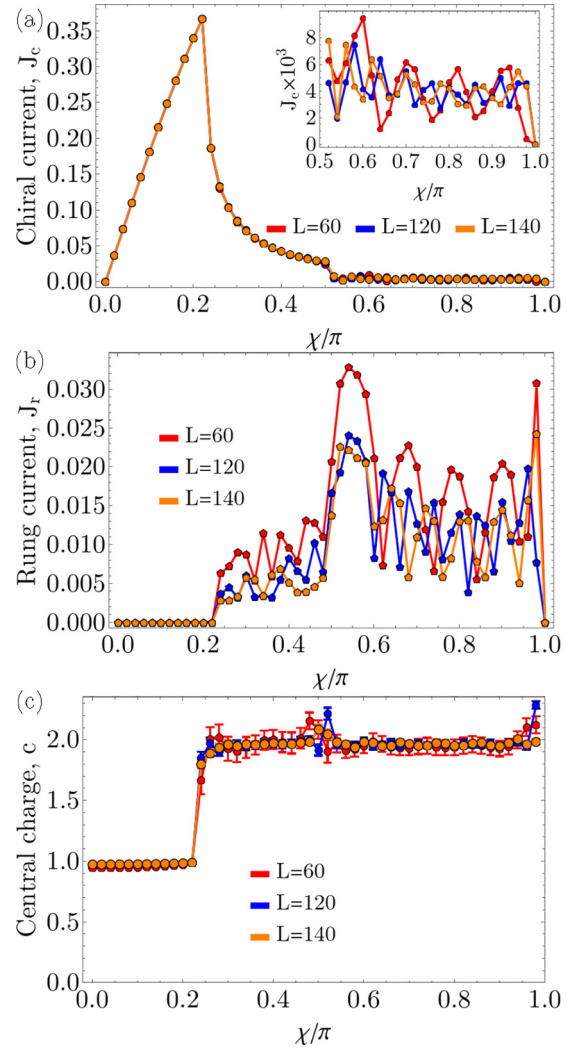


FIG. 12. Numerical ground-state results for (a) the chiral current, J_c , (b) the average rung current, J_r , and (c) the central charge, c , as a function of the flux χ for hard-core bosons, $J_{||}/J = 2$, $\rho = 0.5$, $L \in \{60, 120, 140\}$. We observe a transition between a Meissner superfluid and a vortex superfluid, at $\chi \approx 0.23\pi$. The maximal bond dimension used was $m = 600$ for $L = 60$, and $m = 1200$ for $L = 120$ and $L = 140$.

values are relatively small and show a strong dependence on the size of the system.

In contrast to the regime of finite on-site interaction, here in the vortex phase for $\chi < 0.5\pi$, marked with gray in Fig. 11, we find two peaks in the Fourier transform of the space dependence of the rung currents [Fig. 13(b)]. Above the value $\chi = 0.5\pi$, we find a single peak in the Fourier transform. This implies that vortices of two different lengths coexist in the regime $\chi < 0.5\pi$. We plot the corresponding vortex densities in Fig. 13(a), where one branch corresponds to the expected value $\rho_v \approx \chi$, as discussed in Sec. IV B. The second value of the vortex density seems to be related to the density of the atoms, $\rho_v \approx 0.5\pi = \rho\pi$. We verify the dependence on the density by considering also the case of $\rho = 0.4$ in Fig. 13(c). Here we observe three different peaks, corresponding to $\rho_v \approx \chi$, $\rho_v \approx 0.4\pi = \rho\pi$ up to $\chi = 0.4\pi$, and $\rho_v \approx 0.6\pi = (1 - \rho)\pi$ up to $\chi = 0.6\pi$.

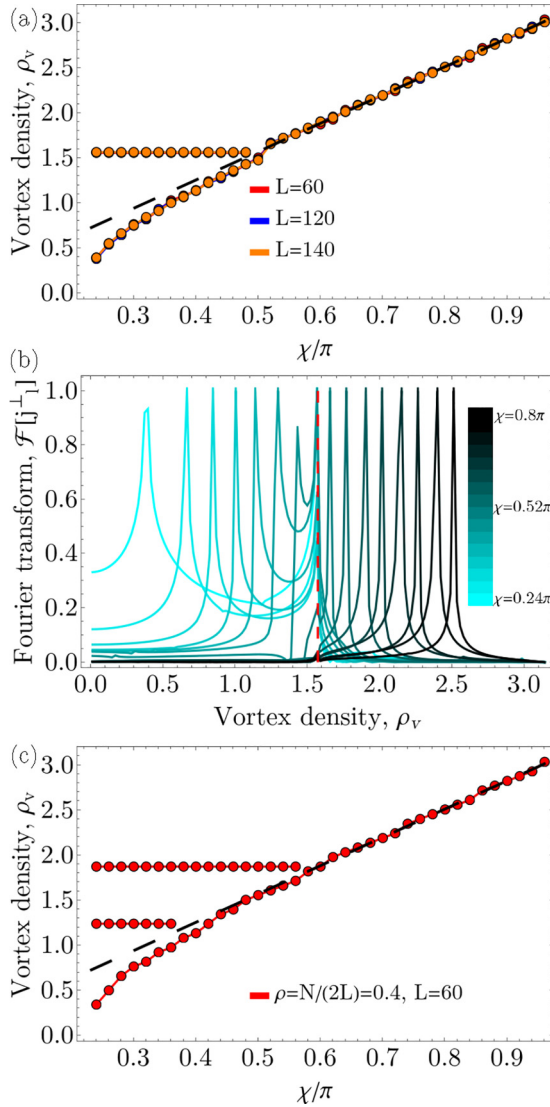


FIG. 13. Numerical ground-state results for (a) the vortex density, ρ_v , at half filling as a function of the flux χ for hard-core bosons, $J_{\parallel}/J = 2$, $\rho = 0.5$, $L \in \{60, 120, 140\}$. (b) The Fourier transform of the rung currents pattern j_i^{\perp} . The sharp peaks correspond to the extracted value of the vortex density. The dashed vertical line marks the value $\rho_v = \pi/2$. The parameters used are $J_{\parallel}/J = 2$, $\rho = 0.5$, $L = 140$, and $0.24\pi \leq \chi \leq 0.8\pi$. (c) The vortex density, ρ_v , at filling $\rho = 0.4$ as a function of the flux χ for hard-core bosons, $J_{\parallel}/J = 2$, $L = 60$. The maximal bond dimension used was $m = 600$ for $L = 60$, and $m = 1200$ for $L = 120$ and $L = 140$.

In the hard-core limit for $\chi = \pi$, the model we consider has been analyzed in Ref. [36]; furthermore, the model can be mapped to a frustrated spin chain, which has been studied in Refs. [64–66]. In the regime of small J_{\parallel}/J a transition from a superfluid phase to a bond order insulator (BOI) has been pointed out. The bond order insulator phase is characterized by a nonzero value of the bond order parameter,

$$O_{\text{BO}} = \frac{1}{2L-1} \sum_j \langle b_{j,1}^{\dagger} b_{j,2} - b_{j+1,1}^{\dagger} b_{j,2} + \text{H.c.} \rangle. \quad (31)$$

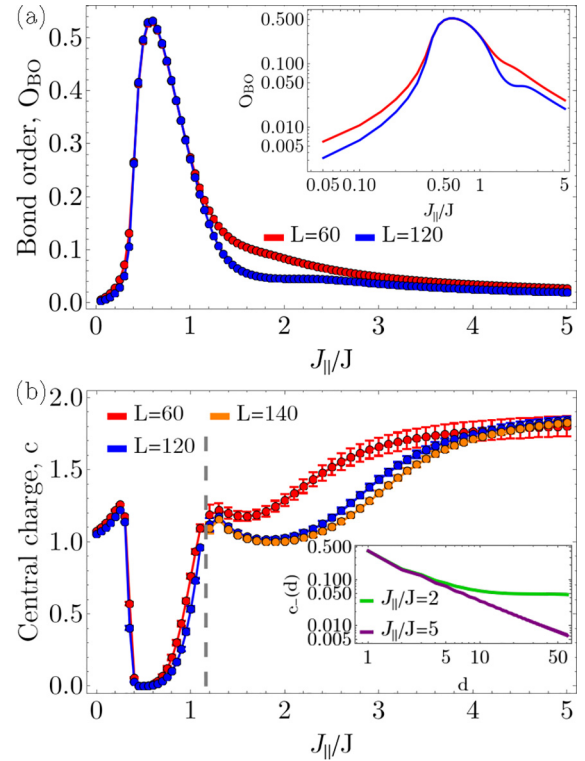


FIG. 14. Numerical ground-state results for (a) the bond order parameter, O_{BO} , and (b) the central charge, c , as a function of J_{\parallel}/J for hard-core bosons, $\chi = \pi$, $\rho = 0.5$, $L \in \{60, 120, 140\}$. For (b) above the vertical gray dashed line, $J_{\parallel}/J \gtrsim 1.2$, we employed finite currents in order to converge to the chiral superfluid phase, with amplitude $j_0/J = 0.25$ (for more details see Appendix D). In the inset of (b) the rung-rung correlations $c_-(d)$ [Eqs. (22)] are plotted as a function of distance in a log-log plot for $J_{\parallel}/J \in \{2, 5\}$ and $L = 120$. We observe a transition from superfluid to bond order insulating state at $J_{\parallel}/J \approx 0.3$, and from the insulating phase to the chiral superfluid at $J_{\parallel}/J \approx 1.2$. For large $J_{\parallel}/J \gtrsim 4$, the system seems to be in a two-mode superfluid; however, the transition shows considerable finite-size effects. The maximal bond dimension used was $m = 600$ for $L = 60$, $m = 1200$ for $L = 120$, and $m = 1500$ for $L = 140$.

We observe the transition to the insulator phase at $J_{\parallel}/J \approx 0.35$, signaled by the finite value of the bond order parameter and $c \approx 0$, as seen Fig. 14.

For $J_{\parallel}/J \gtrsim 1.2$ a phase transition to the chiral superfluid phase is present, equivalent to the transition to the vector chiral phase observed in Refs. [64–66]. In order to converge to the chiral superfluid phase we added a boundary term in the Hamiltonian which explicitly breaks the \mathbb{Z}_2 symmetry and favors the current pattern of the chiral phase (for details see Appendix D). Without the presence of such a term we obtain a state with vanishing currents as seen in Figs. 12(a) and 12(b) for $J_{\parallel}/J = 2$ and Fig. 23 of Appendix D. Up to $J_{\parallel}/J \approx 3$ the numerically computed central charge is consistent with $c = 1$ for the chiral superfluid phase [Fig. 14(b)] and the rung-rung correlations $c_-(d)$ saturate at long distance, as seen in the inset of Fig. 14(b). In contrast, for larger values of J_{\parallel}/J it seems that the central charge has a value of $c \approx 2$ for the finite systems considered, even in the presence of the boundary terms.

Thus, we obtain a state for which both the symmetric and antisymmetric sectors are gapless and identify as a two-mode superfluid. This is supported also by the algebraic decay of the rung-rung correlations $c_-(d)$ on the length scales considered [see inset of Fig. 14(b)]. However, due to important finite-size effects seen in Fig. 14(b) and Fig. 23 of Appendix D, it is not clear from our finite-size results if the two-mode superfluid is present in the thermodynamic limit, or the chiral superfluid will extend to arbitrary large J_{\parallel}/J .

We observe that the bond order parameter remains finite also as we decrease the flux to $\chi < \pi$, as seen in Fig. 15(a) for $J_{\parallel}/J = 0.5$. We can identify a transition between the bond order insulator and a Meissner superfluid for $\chi \approx 0.8\pi$, as the central charge has a jump from $c \approx 0$ to $c \approx 1$ lowering the value of the flux [Fig. 15(c)]. Interestingly, the bond order insulator exhibits finite values of the chiral current for $0.8\pi < \chi < \pi$ as seen in Fig. 15(b), with their pattern similar as in the Meissner phases [see Fig. 4(e)]. This goes beyond the usual phenomenology of the bond order phase and, thus, we name this novel phase the chiral bond order insulator. We note that we observe very little finite-size effects in the values of the chiral currents in increasing the size from $L = 60$ to $L = 180$ [see Fig. 15(b)].

For $J_{\parallel}/J = 0.5$ and $\chi = \pi$ our model corresponds to the Majumdar-Gosh (MG) point [36]. For this point one can write exactly the ground state of the model as a product state

$$|MG\rangle = \prod_j \frac{1}{\sqrt{2}} (|n_{j,1} = 1, n_{j,2} = 0\rangle + |n_{j,1} = 0, n_{j,2} = 1\rangle). \quad (32)$$

In the case of periodic boundary conditions a degenerate state exists, exhibiting the bond order to the rungs connecting the sites $(j + 1, 1)$ and $(j, 2)$. Note that the ground state in this case is not a product of singlets like the usual Majumdar-Gosh state [36]. Thus, in order to gain some insight into the chiral bond order insulator we analyze the Hamiltonian in the case of $J_{\parallel}/J = 0.5$ and small $\chi_0 = \pi - \chi$. The Hamiltonian reads

$$H = -\frac{J}{2} \sum_j (b_j^\dagger b_{j+1} + b_j^\dagger b_{j+1} - b_j^\dagger b_{j+2} + \text{H.c.}) + \frac{J}{2} \chi_0 i \sum_j (-1)^j (b_j^\dagger b_{j+2} - \text{H.c.}), \quad (33)$$

where we used the single-chain representation (see Sec. IV A). The first line of Hamiltonian (33) corresponds to the Majumdar-Gosh points for which the state given in Eq. (32) is the ground state. The second line resembles a current term, which can also be found in the expression of the chiral current. In this limit, the chiral current reads

$$J_c = \frac{J}{2} i \sum_j (-1)^j (b_j^\dagger b_{j+2} - \text{H.c.}) + \frac{J}{2} \chi_0 \sum_j (b_j^\dagger b_{j+2} + \text{H.c.}). \quad (34)$$

In the numerical results we observe that the chiral current shows an algebraic scaling with χ_0 with an exponent of ≈ 2.8 [see the inset of Fig. 15(b)]. This is consistent with the possibility that the term in the second line of Eq. (33) would

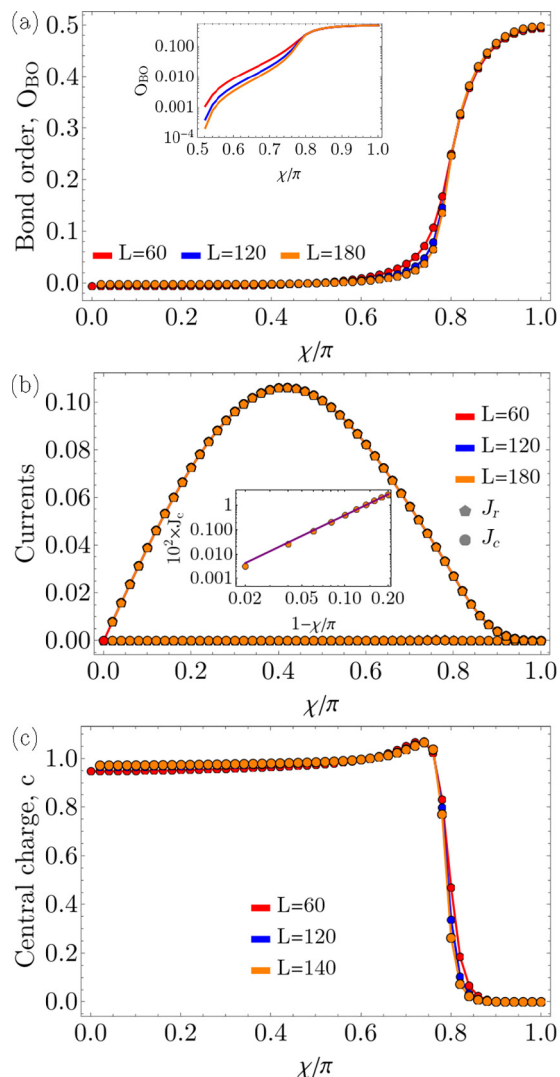


FIG. 15. Numerical ground-state results for (a) the bond order parameter, O_{BO} , (b) the chiral current, J_c , and average rung current, J_r , and (c) the central charge, c , at half filling as a function of the flux χ for hard-core bosons, $J_{\parallel}/J = 0.5$, $\rho = 0.5$, $L \in \{60, 120, 140\}$. In the inset of (a) we plot the bond order parameter for $\chi > 0.5\pi$ in a semilogarithmic plot. In the inset of (b) we show the algebraic scaling of the chiral current, J_c , as a function of $\chi_0 = \pi - \chi$ in a log-log plot. The fitted power law, $\propto (\pi - \chi)^\alpha$, plotted in purple, corresponds to fitted exponent $\alpha = 2.8 \pm 0.02$. We can observe the transition between the Meissner superfluid and the chiral bond order insulator for $\chi \approx 0.8\pi$. The maximal bond dimension used was $m = 600$ for $L = 60$, $m = 1400$ for $L = 120$, and $m = 1800$ for $L = 140$.

produce a higher-order response and induce a finite value of the chiral current.

VI. PHASE DIAGRAM AT UNITY FILLING, $\rho = 1$

In this section, we analyze the phase diagram in the case in which we have a filling of one boson every site, $\rho = 1$. In this case the term $\cos[2p\phi(x)]$, with $p = 1$ [second line of Eq. (9)], or its equivalent in Eq. (12), which stems from the commensurability effects of the interactions, may play an important role. This causes the presence of the Meissner

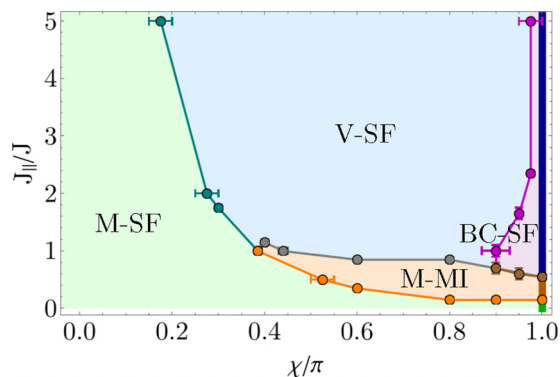


FIG. 16. Sketch of the phase diagram for unity filling, $\rho = 1$, for $U/J = 2.5$. The identified phases (see text) are the Meissner Mott insulator (M-MI), the Meissner superfluid (M-SF), the vortex superfluid (V-SF), and the biased chiral superfluid (BC-SF). At $\chi = \pi$ (marked by a thick vertical line) we have phase transitions between a superfluid phase (green), a Mott insulator (brown), and a chiral superfluid (dark blue).

Mott-insulating (M-MI) phase in the phase diagram, Fig. 16. Besides the presence of the insulating phase, we observe a very similar phase diagram compared to the half-filling case, Fig. 3. Thus, in the following parts of this section we focus on the cuts through the phase diagram which include the Meissner Mott insulator.

In Fig. 17, we show the transition between the Meissner superfluid and the Meissner Mott insulator for $J_{\parallel}/J = 0.5$. In this regime the preferred description is that of a single chain [Eqs. (8) and (9)]. In both phases we have a strong chiral current on the legs of the ladder and no currents on the rungs, Fig. 17(a), with the pattern of currents corresponding to the one depicted in Fig. 4. However, around $\chi \approx 0.5\pi$ we see that the central charge [Fig. 17(b)] goes from a value of $c = 1$ to $c = 0$, signaling the transition to the insulating phase. As the Meissner Mott insulator is a fully gapped phase one expects that $c = 0$. Furthermore, the single-particle correlations decay exponentially in this phase, as seen in the inset of Fig. 17(b) for $\chi = 0.56\pi$.

Similarly to the half-filling case (Sec. IV), by increasing J_{\parallel}/J we can also obtain the vortex superfluid phase (see Fig. 16). In Fig. 18, for $J_{\parallel}/J = 1$, we observe that for $\chi \lesssim 0.45$ we have a strong chiral current and no currents on the rungs, signaling the Meissner superfluid phase up to $\chi \lesssim 0.39\pi$ and the Meissner Mott insulator for $0.39\pi \lesssim \chi \lesssim 0.45\pi$, as the central charge changes from $c \approx 1$ to $c \approx 0$ around $\chi \approx 0.39\pi$. At $\chi \approx 0.45\pi$ a transition to the vortex superfluid occurs, as the central charge becomes $c \approx 2$ and the rung currents are finite. For large values of the flux, $\chi \gtrsim 0.9\pi$, we enter the biased chiral superfluid phase, which shows a finite density imbalance [Fig. 18(c)]. The biased phase is present up to large values of J_{\parallel}/J for χ close to π (Fig. 16).

At large J_{\parallel}/J for $\chi = \pi$ we obtain the chiral superfluid phase, for which $c = 1$, and the correlations c_{-} and c_{\parallel} saturate at a finite value at large distances indicating the strong currents present on both the rungs and legs of the ladder (see Fig. 19). As we decrease J_{\parallel}/J a transition to a Mott-insulator phase is

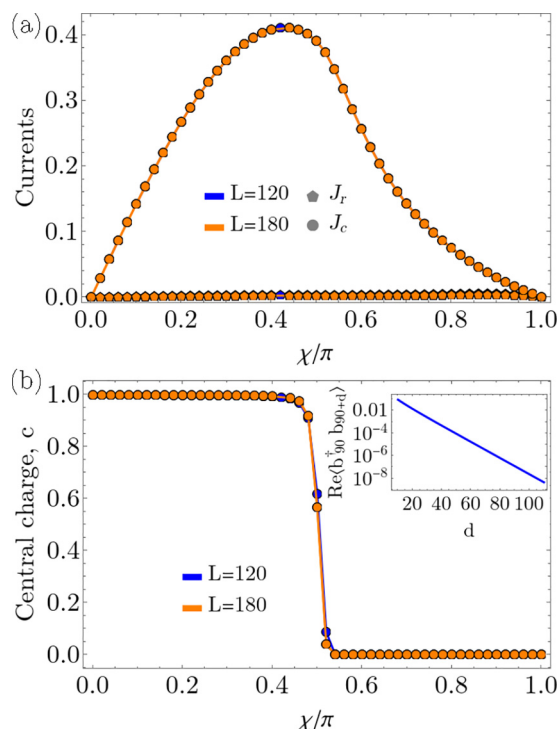


FIG. 17. Numerical ground-state results for (a) the average rung current, J_r , and the chiral current, J_c , and (b) the central charge, c , as a function of the flux χ for $J_{\parallel}/J = 0.5$, $U/J = 2.5$, $\rho = 1$, and $L \in \{120, 180\}$. The inset of (b) contains the exponential decay with distance of the single-particle correlations for $\chi = 0.56\pi$ and $L = 180$. We can identify a transition from the Meissner superfluid to the Meissner Mott insulator around $\chi \approx 0.5\pi$. The maximal bond dimension used was $m = 1200$ for $L = 120$ and $m = 1800$ for $L = 180$.

present at $J_{\parallel}/J \approx 0.6$, as seen in the vanishing value of the central charge $c = 0$ [Fig. 19(a)]. For a value of $J_{\parallel}/J = 0.1$ the central charge is close to one, signaling the superfluid phase.

VII. DISCUSSION

In this section, we discuss the obtained phase diagrams in comparison with the phases seen in square ladders, with an emphasis on the phases specific to the triangular ladder. To recall the phase diagrams see Fig. 3 for $\rho = 0.5$, Fig. 11 for $\rho = 0.5$ and hard-core bosons, and Fig. 16 for $\rho = 1$.

At small values of the flux, $\chi \lesssim 0.6\pi$, the behavior is essentially similar to the one of square ladders and exhibits a phase transition between Meissner and vortex states [3]. We obtain both the superfluid and Mott-insulator states with Meissner character. However, whether vortex Mott-insulating phases can be observed in the triangular ladder, as in the square ladder [11,19], remains an open question. For hard-core bosons, we identify an effect occurring in the vortex phase, namely, the presence of a second frequency peak in the Fourier transform of the pattern of rung currents, which seems to be commensurate with the bosonic density. The explanation of such a harmonic is unclear at the moment and will clearly deserve further studies.

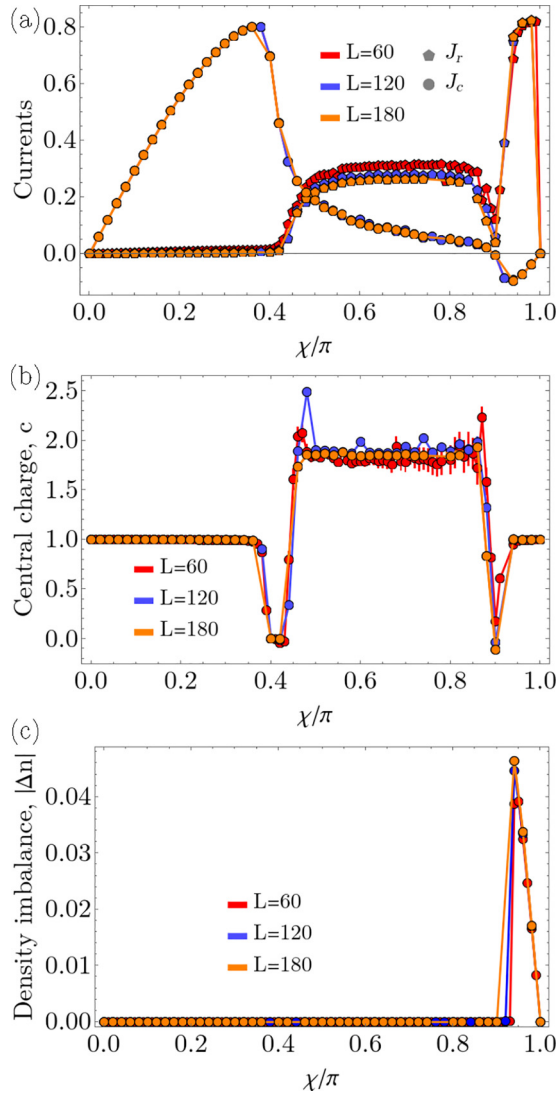


FIG. 18. Numerical ground-state results for (a) the average rung current, J_r , and the chiral current, J_c , (b) the central charge, c , and (c) the absolute value of the density imbalance, $|\Delta n|$, as a function of the flux χ for $J_{||}/J = 1$, $U/J = 2.5$, $\rho = 1$, and $L \in \{60, 120, 180\}$. We observe the following sequence of phases: Meissner superfluid, Meissner Mott insulator, vortex superfluid, and biased chiral superfluid. The maximal bond dimension used was $m = 600$ for $L = 60$, $m = 1200$ for $L = 120$, and $m = 1800$ for $L = 180$.

Contrary to what happens for small flux, at large values of χ , the frustration induced by the triangular nature of the hopping becomes more prominent and novel phases appear. One phase without an equivalent on the square ladder is the chiral bond order insulator, which we obtained in the hardcore limit. This phase is different from other states exhibiting bond ordering due to its finite chiral current flowing on the legs of the triangular ladder. This bond-ordered phase does not stem from a band-insulator limit for small $J_{||}/J$, as, for example, the Meissner Mott insulator present at half filling for a square ladder [15]. This can be inferred from the fact that at small $J_{||}/J$ we have a transition to a Meissner superfluid, or superfluid for $\chi = \pi$ (see Fig. 11).

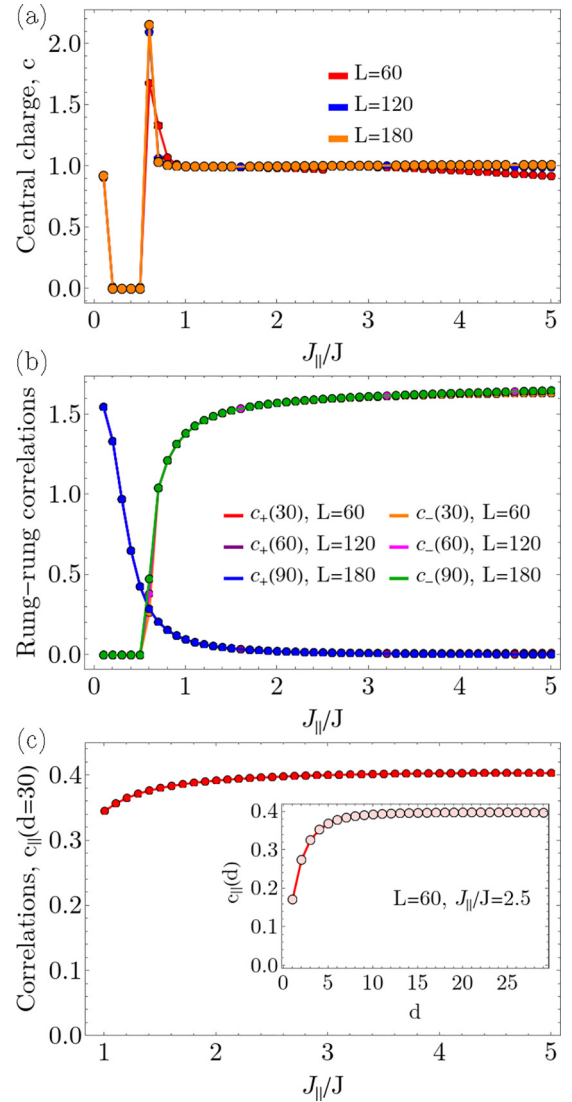


FIG. 19. Numerical ground-state results for (a) the central charge, (b) the saturation value of the rung-rung correlations c_{\pm} [Eqs. (22)], (c) the saturation value of the current-current correlations on the legs, $c_{||}$ [Eq. (23)], as a function of $J_{||}$, for $\chi = \pi$, $U/J = 2.5$, $\rho = 1$, and $L \in \{60, 120, 180\}$. In the inset of (c) we show the distance dependence of $c_{||}(d)$ at $J_{||}/J = 2.5$. We observe a transition from superfluid to Mott insulator states at $J_{||}/J \approx 0.15$, and from the insulating phase to the chiral superfluid at $J_{||}/J \approx 0.6$. The maximal bond dimension used was $m = 500$ for $L = 60$, $m = 1200$ for $L = 120$, and $m = 1500$ for $L = 180$.

At finite values of the on-site interaction we find another phase specific to the triangular ladder: the biased chiral superfluid, a phase breaking the discrete \mathbb{Z}_2 symmetry of the ladder. Even though in the weakly interacting limit this phase can be understood as the condensation of the bosons in a single minimum of the double minima potential, similarly to the biased ladder phase appearing in the square ladder [12,18,19], the nature of its currents is very different. The biased phase of the square ladder exhibits Meissner-like currents, but the biased chiral superfluid is closely related to the chiral superfluid present at $\chi = \pi$. Thus, due to the frustration for χ close to π , the symmetric and antisymmetric sectors are coupled,

such that a gapped antisymmetric sector implies a finite value of the expectation value of the gradient of the symmetric field, $\langle \partial_x \theta_s \rangle$. This mechanism induces strong currents flowing on opposite direction on the rungs and legs of the triangular ladder [see Figs. 4(c) and 4(d)].

One interesting direction left open by our study is the investigation of the behavior of the phases with increasing interaction strength. In particular, there is the question at $\rho = 0.5$ on how to connect the phase diagram for $U/J = 2.5$ (Fig. 3) and the phase diagram for $U/J \rightarrow \infty$ (Fig. 11). Our preliminary numerical data show that the chiral bond order insulator extends to finite interactions, as low as $U/J \approx 10$ for $J_{\parallel}/J = 0.5$ and $\chi = 0.95\pi$, where a phase transition to the biased chiral superfluid might be present. As the extent of the biased chiral superfluid seems to diminish as we increase U , it would be interesting to see if the phase will be suppressed at a critical value of the interaction, or if it survives up to the hard-core $U \rightarrow \infty$ limit. Furthermore, in the case of $\rho = 1$, as we expect the Meissner Mott insulator to have covered a larger region of the phase diagram as we increase U , the question arises if any other phases remain stable at very large interaction strengths.

Ultracold atoms in optical lattices provide an experimental platform for the study of such low-dimensional systems in the presence of an artificial gauge field. The flux has been implemented with time-dependent modulations [67], laser-assisted Raman hopping [68–70], or synthetic dimensions [33–35, 71, 72]. Combining these techniques with triangular optical lattices [47, 48] offers the possibility of the experimental realization of the model we studied.

In order to distinguish the different ground-state phases one could perform different measurements. From *in situ* measurements one could access the local densities and currents [73], and the momentum distribution can be obtained via time-of-flight measurements. In the case of square ladders, in Ref. [6], Atala *et al.* used a measurement scheme involving the projection onto double wells to measure the chiral current. The biased chiral superfluid phase seems to be robust for densities away from half filling; thus, it should be possible to observe it also in the case of a parabolic trapping potential. However, for the bond-ordered states, having one particle every two sites is important.

VIII. CONCLUSIONS

In this work, we investigated the phase diagram of interacting bosonic atoms confined to a two-leg triangular ladder in an artificial gauge field. We showed the existence of Meissner phases both in the superfluid (M-SF) and in the Mott-insulator (M-MI) regimes and of incommensurate vortex superfluid (V-SF) phases, which are similar to the states obtained in square ladders with a flux. However, we have seen that at large values of the flux the frustration effects of the triangular geometry play a crucial role and several phases are realized. For finite on-site interaction a biased chiral superfluid (BC-SF) phase which breaks the \mathbb{Z}_2 symmetry of the ladder and exhibits an imbalanced density on the two legs of the ladder is present. It has a similar current pattern with the chiral superfluid (C-SF) phase which is obtained as the $\chi \rightarrow \pi$ limit of the biased phase. We study the transition from the chiral superfluid to

the superfluid phase by performing an interpolation between the $\chi = \pi$ triangular ladder and the square ladder. In the case of hard-core bosons, we show the presence of a chiral bond order insulator (C-BOI) phase, which corresponds to a finite value of the bond order parameter and exhibits Meissner-like currents.

Our work paves the way for studies of the triangular ladder with an artificial gauge field in nonequilibrium settings. This can be envisioned either in the context of the Hall effect [31, 32], or by the coupling to an external environment [74–78].

ACKNOWLEDGMENTS

We thank M. Aidelsburger, L. Pizzino, and L. Tarruell for stimulating discussions. We are grateful to S. Furukawa for pointing out the presence of the chiral superfluid phase in the hard-core case and for enlightening discussions on that point. This work was supported by the Swiss National Science Foundation under Division II grant 200020-188687.

APPENDIX A: NONINTERACTING LIMIT

We diagonalize the kinetic part of the Hamiltonian,

$$H_{\text{kin}} = H_{\perp} + H_{\parallel}, \quad (\text{A1})$$

by performing the Fourier transforms on the two legs:

$$b_m(k) = \frac{1}{\sqrt{L}} \sum_j e^{ikj} b_{j,m}. \quad (\text{A2})$$

The Hamiltonian in momentum space reads

$$\begin{aligned} H_{\text{kin}} = & \sum_k \{ -2J_{\parallel} \cos(k + \chi) b_1^{\dagger}(k) b_1(k) \\ & - 2J_{\parallel} \cos(k - \chi) b_2^{\dagger}(k) b_2(k) \\ & - J[(1 + e^{ik}) b_1^{\dagger}(k) b_2(k) + (1 + e^{-ik}) b_2^{\dagger}(k) b_1(k)] \}. \end{aligned} \quad (\text{A3})$$

The eigenvalues of this quadratic Hamiltonian are

$$\begin{aligned} E_{\pm}(\chi) = & -2J_{\parallel} \cos(k) \cos(\chi) \\ & \pm \sqrt{2J^2 [1 + \cos(k)] + 4J_{\parallel}^2 \sin^2(k) \sin^2(\chi)}. \end{aligned} \quad (\text{A4})$$

The energy bands are plotted in Fig. 2.

If we compare these bands with the ones obtained for the square lattice of the double of the flux,

$$\begin{aligned} E_{\pm}^{\text{square}}(2\chi) = & -2J_{\parallel} \cos(k) \cos(\chi) \\ & \pm \sqrt{J^2 + 4J_{\parallel}^2 \sin^2(k) \sin^2(\chi)}, \end{aligned} \quad (\text{A5})$$

we observe that in the limit of large J_{\parallel} they become very similar. Thus, one can expect in this regime analogous behaviors in the two setups.

APPENDIX B: LUTTINGER PARAMETER IN THE SINGLE-CHAIN LIMIT

For a Bose-Hubbard chain [Eqs. (8) and (9)] one can numerically compute the Luttinger parameter of the superfluid

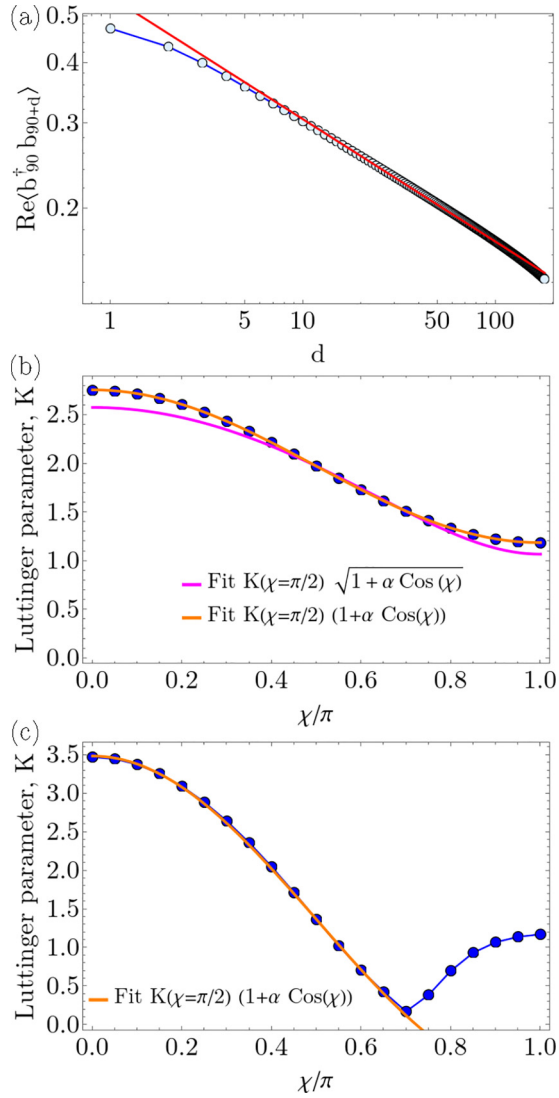


FIG. 20. (a) The decay of the single-particle correlations, $\text{Re}\langle b_{90}^\dagger b_{90+d} \rangle$, in the Meissner superfluid, for $\chi = 0.5\pi$, $J_{\parallel}/J = 0.2$, $U/J = 2.5$, $N/2L = 0.5$, and $L = 180$. The algebraic fit follows Eq. (B1) and corresponds to the fitted value of $K = 1.973 \pm 0.005$. [(b), (c)] The dependence of the Luttinger parameter K as a function of the flux χ , for (b) $J_{\parallel}/J = 0.2$, (c) $J_{\parallel}/J = 0.5$, $U/J = 2.5$, $L = 60$, and $N/2L = 0.5$. The solid curves correspond to fitting $K(\chi = \pi/2) + \alpha \cos(\chi)$ [Eq. (B3)] (orange) and $K(\chi = \pi/2)\sqrt{1 + \alpha \cos(\chi)}$ [Eq. (B4)] (magenta).

phase by looking at the algebraic decay of the single-particle correlations [1],

$$\langle b^\dagger(x)b(0) \rangle \propto x^{-1/(2K)}, \quad (\text{B1})$$

where x is the lattice position in the continuum limit. In Fig. 20(a) we show the decay of the single-particle correlations for parameters corresponding the Meissner superfluid phase and its algebraic fit.

In Eq. (9) we saw that the effective Luttinger parameter of the model depends on the value of the flux,

$$u_{\text{eff}}K_{\text{eff}} = uK + t_{\parallel} \cos(\chi) \quad (\text{B2})$$

$$\frac{u_{\text{eff}}}{K_{\text{eff}}} = \frac{u}{K},$$

where $t_{\parallel} \equiv 16\pi\rho J_{\parallel}$, which leads to the following dependence on the flux:

$$K_{\text{eff}} = K \sqrt{1 + \frac{t_{\parallel}}{uK} \cos(\chi)}. \quad (\text{B3})$$

However, the numerical results seem to deviate from this dependence for the values of the flux close to the maxima of $|\cos(\chi)|$, Fig. 20. Furthermore, we observe that the numerical data follow

$$K_{\text{eff}} = K + \alpha \cos(\chi), \quad (\text{B4})$$

as seen in Fig. 20(b). We note that the discrepancy between the two dependencies becomes smaller if we consider smaller values of t_{\parallel} .

In the case the long-range hopping in the chain is strong enough, $t_{\parallel} > uK$, for large values of the flux the prefactor $uK + t_{\parallel} \cos(\chi)$ can become zero or negative, signaling an instability. We observe the approach towards zero also in the dependence of the numerically extracted Luttinger parameter. This marks the phase transition between the Meissner superfluid to the biased phase.

APPENDIX C: MEAN-FIELD APPROACH FOR THE \mathbb{Z}_2 -SYMMETRY-BROKEN PHASE

Starting from the Hamiltonian derived in Sec. IV C,

$$H = H_0 + H_{\perp},$$

$$H_0 = \int \frac{dx}{2\pi} \left[uK \partial_x \theta_s(x)^2 + \frac{u}{K} \partial_x \phi_s(x)^2 \right] + \int \frac{dx}{2\pi} \left[uK \partial_x \theta_a(x)^2 + \frac{u}{K} \partial_x \phi_a(x)^2 \right],$$

$$H_{\perp} = -t_{\perp} \int dx \sin(\sqrt{2}\theta_a), \quad (\text{C1})$$

where $t_{\perp} = \sqrt{2}\rho J$, we want to investigate the effect of the H_{\perp} term which couples the symmetric and antisymmetric sectors. For this, we follow the self-consistent mean-field procedure described in Ref. [63] for frustrated spin ladders.

We perform the mean-field decoupling of H_{\perp} to obtain the following mean-field Hamiltonian density:

$$\mathcal{H}_{\text{MF}} = \mathcal{H}_0 + k \partial_x \theta_s - \mu \Lambda \sin(\sqrt{2}\theta_a), \quad (\text{C2})$$

where we have assumed that the ground state of the system has a nonzero current $\partial_x \theta_s$. The self-consistency conditions are given by

$$k = -t_{\perp} \langle \sin(\sqrt{2}\theta_a) \rangle,$$

$$\mu \Lambda = t_{\perp} \langle \partial_x \theta_s \rangle. \quad (\text{C3})$$

One can observe that \mathcal{H}_{MF} decomposes in two independent parts:

$$\mathcal{H}_s = uK \partial_x \theta_s(x)^2 + \frac{u}{K} \partial_x \phi_s(x)^2 + \partial_x \theta_s,$$

$$\mathcal{H}_a = uK \partial_x \theta_a(x)^2 + \frac{u}{K} \partial_x \phi_a(x)^2 - \mu \Lambda \sin(\sqrt{2}\theta_a). \quad (\text{C4})$$

In the symmetric sector we can arrive at a quadratic Hamiltonian by performing the following redefinition of the field:

$\theta_s(x) \rightarrow \theta_s(x) - \frac{k}{2uK}x$. The average value of $\theta_s(x)$ is, thus, given by

$$\langle \partial_x \theta_s(x) \rangle = -\frac{k}{2uK}. \quad (\text{C5})$$

The Hamiltonian for the antisymmetric sector is a sine-Gordon model for the field θ_a ; this can be solved exactly and the value of the mass is given by [1]

$$\langle \sin(\sqrt{2}\theta_a) \rangle = c \left(\frac{\mu}{uK\Lambda} \right)^{\frac{1}{4K-1}}, \quad (\text{C6})$$

where c is a constant, which can be calculated [79]. Inserting the expectation values from Eqs. (C5) and (C6) in Eq. (C3) we obtain the solutions

$$\begin{aligned} \mu &= \tilde{c} t_{\perp}^{\frac{4K-1}{2K-1}} (uK\Lambda)^{-\frac{2K}{2K-1}}, \\ k &= -2\tilde{c} t_{\perp}^{\frac{2K}{2K-1}} (uK\Lambda)^{-\frac{1}{2K-1}}, \end{aligned} \quad (\text{C7})$$

where \tilde{c} is a constant. In the regime in which the solutions are valid the field θ_a is fixed to the minima of the sine-Gordon potential, $\langle \theta_a \rangle = \frac{\pi}{2\sqrt{2}}$, and the mass in the antisymmetric sector scales as $\langle \sin(\sqrt{2}\theta_a) \rangle \propto t_{\perp}^{\frac{1}{2K-1}}$.

The Hamiltonian from which we started, Eq. (C1), has a \mathbb{Z}_2 symmetry as the Hamiltonian remains invariant under the following change of signs, $\partial_x \theta_s \rightarrow -\partial_x \theta_s$ and $\sin(\sqrt{2}\theta_a) \rightarrow -\sin(\sqrt{2}\theta_a)$, which changes the expectation value of the field, $\langle \theta_a \rangle = \frac{\pi}{2\sqrt{2}} \rightarrow \langle \theta_a \rangle = \frac{3\pi}{2\sqrt{2}}$. This implies that changing the signs in the mean-field solution still satisfies the self-consistency conditions (C3). Thus, we obtain that in the regime in which the self-consistency conditions have solutions the ground state is given by two degenerate states which break the \mathbb{Z}_2 symmetry.

The solutions of the self-consistency conditions (C7) can be obtained when $K > 0.5$. However, in the numerical results, around the phase transition between the superfluid and the chiral superfluid, $0.23 \lesssim J_{\parallel}/J \lesssim 0.47$, we obtain a $K < 0.5$ also in the chiral superfluid phase [see Fig. 21(a)]. We compute numerically K from the decay of the single-particle correlations [see Figs. 21(b) and 21(c)]. We attribute this discrepancy to the fact that we numerically observe $K > 0.5$ for small values of J_{\parallel} , for which the approach of considering the system as two coupled chains might not be valid.

Using the mean-field results we can compute the scaling of the single-particle correlations along one of the legs of the ladder,

$$\begin{aligned} \langle b_{0,1}^{\dagger} b_{j,1} \rangle &\propto \langle e^{i(\theta_1(x) - \theta_1(0))} \rangle \\ &\propto x^{-\frac{1}{4K}} e^{-i\frac{k}{2\sqrt{2}uK}x}, \end{aligned} \quad (\text{C8})$$

where we can see that the correlations exhibit incommensurate oscillations. We plotted the numerical behavior of the correlations in Figs. 21(b) and 21(c) for two values of J_{\parallel}/J in the chiral superfluid phase. We observe that the scaling of Eq. (C8) agrees very well with the numerical results.

In the rest of this section we extend the mean-field approach to the Hamiltonians (28) and (29) we used to

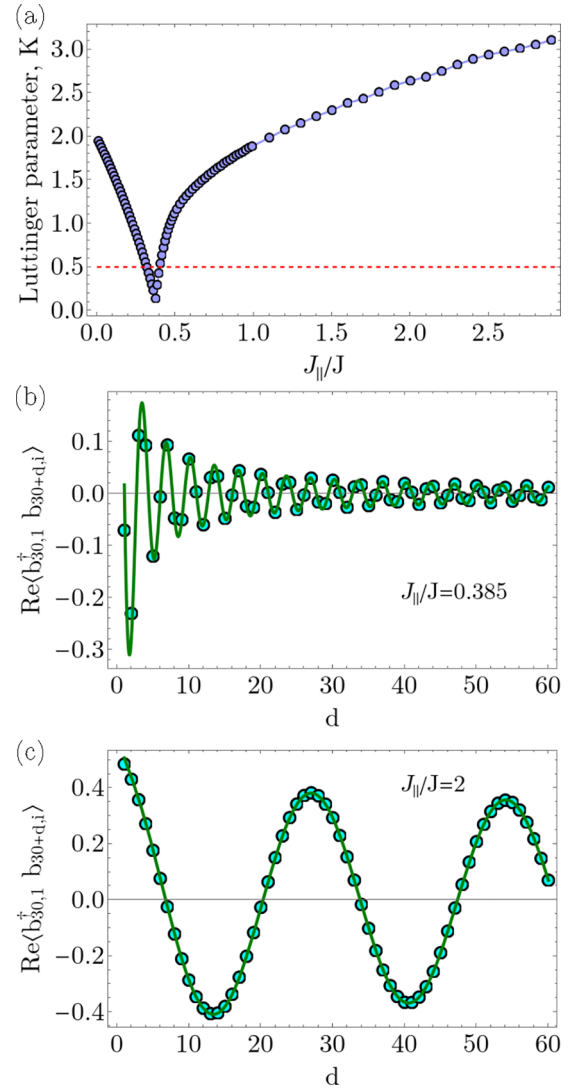


FIG. 21. (a) The dependence of the Luttinger parameter K on J_{\parallel}/J for $\chi = \pi$, $U/J = 2.5$, $N/2L = 0.5$, and $L = 120$. We extract K from the decay of the single-particle correlations, using Eq. (B1) in the superfluid phase, $J_{\parallel}/J \lesssim 0.37$, and Eq. (C8) in the chiral superfluid phase, $J_{\parallel}/J \gtrsim 0.37$. The dashed red line corresponds to $K = 0.5$. [(b), (c)] The decay of the single-particle correlations, $\text{Re}\langle b_{30,1}^{\dagger} b_{30+d,i} \rangle$, in the chiral superfluid for (b) $J_{\parallel}/J = 0.385$ and (c) $J_{\parallel}/J = 2$. The solid line corresponds to a fit with the functional form of Eq. (C8); the fitted Luttinger parameters are (b) $K = 0.294 \pm 0.001$ and (c) $K = 2.64 \pm 0.01$.

investigate the interpolation to the square ladder in Sec. IV E:

$$\begin{aligned} H &= H_0 + H_{\perp}, \\ H_0 &= \int \frac{dx}{2\pi} \left[uK \partial_x \theta_s(x)^2 + \frac{u}{K} \partial_x \phi_s(x)^2 \right] \\ &\quad + \int \frac{dx}{2\pi} \left[uK \partial_x \theta_a(x)^2 + \frac{u}{K} \partial_x \phi_a(x)^2 \right], \\ H_{\perp} &= -t_{\perp} \int dx \sin(\sqrt{2}\theta_a) \partial_x \theta_s \\ &\quad - \tilde{t} \int dx \cos(\sqrt{2}\theta_a), \end{aligned} \quad (\text{C9})$$

where $\tilde{t} = 2\rho t$. The mean-field decoupling is performed in the same manner as previously and the self-consistency conditions are the same as in Eq. (C3). The difference arises in the potential present in the antisymmetric Hamiltonian density,

$$\begin{aligned} \mathcal{H}_a &= uK\partial_x\theta_a(x)^2 + \frac{u}{K}\partial_x\phi_a(x)^2 \\ &\quad - \mu\Lambda \sin(\sqrt{2}\theta_a) - \tilde{t} \cos(\sqrt{2}\theta_a) \\ &= uK\partial_x\theta_a(x)^2 + \frac{u}{K}\partial_x\phi_a(x)^2 \\ &\quad - \sqrt{(\mu\Lambda)^2 + \tilde{t}^2} \sin(\sqrt{2}\theta_a + \psi), \end{aligned} \quad (\text{C10})$$

with the phase $\psi = \arctan(\frac{\mu\Lambda}{\tilde{t}})$. The mass in the sine-Gordon model is given by [1]

$$\langle \sin(\sqrt{2}\theta_a + \psi) \rangle = c \left(\frac{\sqrt{(\mu\Lambda)^2 + \tilde{t}^2}}{uK\Lambda} \right)^{\frac{1}{4K-1}}. \quad (\text{C11})$$

This leads to the self-consistent solution

$$(\mu\Lambda)^2 = \tilde{c}_1 t_{\perp}^{\frac{8K-2}{2K-1}} - \tilde{t}^2. \quad (\text{C12})$$

The mean-field approach allows us to compute the scaling with the coupling constants of the following expectation values:

$$\begin{aligned} \langle \sin(\sqrt{2}\theta_a) \rangle &\propto t_{\perp}^{-2} \sqrt{\tilde{c}_1 t_{\perp}^{\frac{8K-2}{2K-1}} - \tilde{t}^2}, \\ \langle \sin[\sqrt{2}\theta_a(x \rightarrow \infty)] \sin[\sqrt{2}\theta_a(0)] \rangle &\propto t_{\perp}^{-4} (\tilde{c}_1 t_{\perp}^{\frac{8K-2}{2K-1}} - \tilde{t}^2), \\ \langle \cos(\sqrt{2}\theta_a) \rangle &\propto \tilde{t} t_{\perp}^{-2}, \\ \langle \cos(\sqrt{2}\theta_a(x \rightarrow \infty)) \cos(\sqrt{2}\theta_a(0)) \rangle &\propto \tilde{t}^2 t_{\perp}^{-4}. \end{aligned} \quad (\text{C13})$$

APPENDIX D: NUMERICAL RESULTS IN THE \mathbb{Z}_2 -SYMMETRY-BROKEN PHASES

In this section, we briefly discuss the challenges of the numerical convergence in the cases in which we have two degenerate ground states due to the breaking of the \mathbb{Z}_2 symmetry. The DMRG algorithm can in principle converge to any state of the two-dimensional ground-state manifold; this can increase the difficulty of the identification of the nature of the phases. In this work we identified two such phases, the chiral superfluid for $\chi = \pi$ (see Sec. IV C) and the biased chiral superfluid for small values of $\chi_0 = \pi - \chi$. (see Secs. IV A and IV D).

The difficulties of interpreting the numerical results for the average rung current are apparent when the ground-state search algorithm uses the Hamiltonian in the leg gauge [Eq. (16)] for $\chi = \pi$ and $L = 60$ as seen in Fig. 22(a). For these parameters we identified in Sec. IV C a phase transition between the superfluid and chiral superfluid phases at $J_{\parallel}/J \approx 0.3$. However, the rung current [red points in Fig. 22(a)] seems to indicate two transitions at $J_{\parallel}/J \approx 0.7$ and $J_{\parallel}/J \approx 2$, which we do not expect based on our analytical consideration. This behavior can be explained by the possibility that for $0.7 \lesssim J_{\parallel}/J \lesssim 2$ we numerically converge to one of the chiral states with strong currents described in Appendix C and for the other values of J_{\parallel}/J to an equal superposition of the two states with

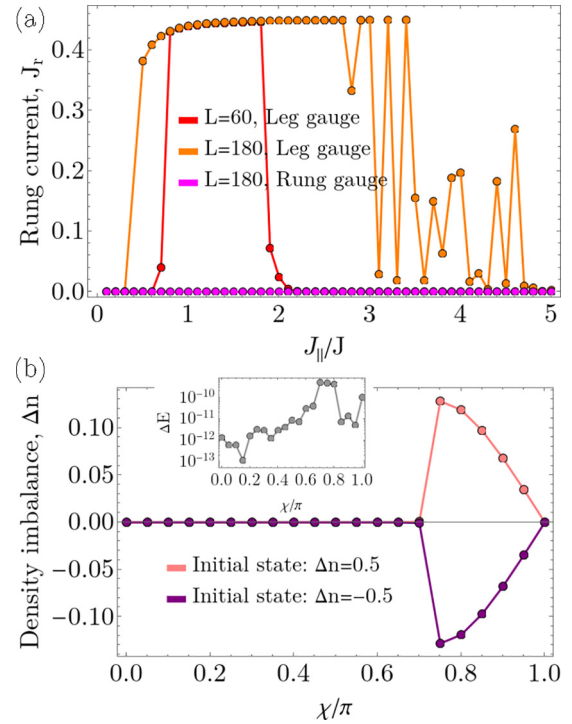


FIG. 22. (a) The average rung current, J_r , as a function of J_{\parallel}/J for two system sizes, $L = 60$ and $L = 180$. The numerical simulations were done with the Hamiltonian either in the leg gauge or in the rung gauge (see main text, Sec. IV C). The parameters used are $\chi = \pi$, $U/J = 2.5$, and $N/2L = 0.5$. (b) The density imbalance, Δn , as a function of the flux χ for two different initial states used in the numerical DMRG simulations. The inset contains the energy difference, ΔE , between the two numerical results. The parameters used are $J_{\parallel}/J = 0.5$, $U/J = 2.5$, $N/2L = 0.5$, and $L = 60$.

opposite current patterns. Furthermore, if we analyze a large system, $L = 180$, in the same gauge we observe that at large J_{\parallel}/J the values obtained for the rung current seem to strongly depend on the value of J_{\parallel}/J [orange points in Fig. 22(a)], which would imply that for each point we obtain different weights of the superposition.

On the other hand, in the rung gauge (17), we converge to a state with zero currents for all parameters considered [magenta points in Fig. 22(a)]. This is consistent with an equal superposition of the two states with opposite current patterns. We note that we used the rung gauge for the results at $\chi = \pi$ presented in the main text. Thus, in order to be able to identify the chiral superfluid phase in a confident manner, based on the insights obtained from the mean-field approach of Appendix C, we computed in Sec. IV C the rung-rung correlations [Eqs. (22)] and current-current correlations along the legs [Eq. (23)] which have the same value for any state in the ground-state manifold.

Furthermore, we analyze the effect of the initial states in the ground-state search algorithm. We observe in Fig. 22(b) that in the region in which we identified the biased chiral superfluid in Sec. IV A the value of the density imbalance depends on the initial state. Here we used as an initial state a product state in which all atoms were either on the first leg, $\Delta n = 0.5$, or on the second leg, $\Delta n = -0.5$. Furthermore,

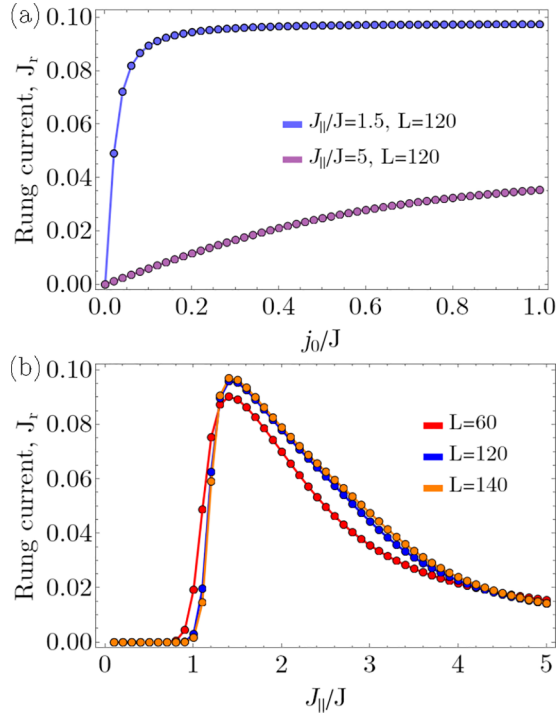


FIG. 23. The average rung current, J_r , computed in the middle half of the system for hard-core bosons, (a) as a function of the strength of the boundary currents j_0/J [Eq. (D1)] for $J_{\parallel}/J \in \{1.5, 5\}$; (b) as a function of J_{\parallel}/J for $L \in \{60, 120, 140\}$, with finite boundary currents $j_0/J = 0.25$. The parameters used are $\chi = \pi$, $U/J \rightarrow \infty$, and $\rho = 0.5$. The maximal bond dimension used was $m = 600$ for $L = 60$, $m = 1200$ for $L = 120$, and $m = 1500$ for $L = 140$.

the two numerically obtained states have the same energy as seen in the inset of Fig. 22(b). Our implementation of the DMRG algorithm guarantees the convergence of the ground-state energy up to 10^{-8} . We note that the results presented in Fig. 22(b) do not imply that we converged to the state with a maximal (or minimal) value of the density imbalance.

However, it does show that we obtained two distinct states in the ground-state manifold which supports the conclusion that we break the \mathbb{Z}_2 symmetry in this regime.

An approach to facilitate the convergence of the DMRG algorithm to one of the \mathbb{Z}_2 -symmetry-broken states is to add a term in the Hamiltonian that breaks the symmetry. Afterwards, one extrapolates the results in the limit of strength of the symmetry-breaking term going to zero. For example, in order to identify the chiral superfluid phase for hard-core bosons at $\chi = \pi$ in Sec. V [see Fig. 14(b)], we employed the following term in the simulations [written in the single-chain representation, Eq. (8)]:

$$H_b = -ij_0 \left(\sum_{j=1}^3 + \sum_{j=L-3}^{L-1} \right) (b_j^\dagger b_{j+1} - b_{j+1}^\dagger b_j), \quad (\text{D1})$$

which favors the rung current pattern realized in the chiral superfluid and biased chiral superfluid phases at the boundaries of the system. In Fig. 23 we analyze the behavior of the currents around the chiral superfluid phase when using boundary currents in the simulations. The average rung current in the bulk of the system, computed in the middle half, as a function of j_0/J is shown in Fig. 23(a). We can observe that for $J_{\parallel}/J = 1.5$ the rung current rapidly saturates with increasing j_0/J , and, thus, we can be confident in the presence of the chiral superfluid phase by extrapolating in the limit of $j_0/J \rightarrow 0$. However, for $J_{\parallel}/J = 5$ the extrapolation seems to rather indicate a state without currents. In Fig. 23(b) we show the average rung current in the bulk of the ladder as a function of J_{\parallel}/J for a fixed strength of $j_0/J = 2.5$. We observe that for $1.2 \lesssim J_{\parallel}/J \lesssim 4$, the rung current increases with increasing the system size, we attribute this behavior to the presence of the chiral superfluid phase (see Sec. V). It is not easy, for the considered system sizes and value of j_0/J , to distinguish in Fig. 23(b) if a phase transition to a two-mode superfluid occurs above $J_{\parallel}/J \gtrsim 4$. For this a careful analysis of the extrapolation and system size dependence is needed.

-
- [1] T. Giamarchi, *Quantum Physics in One Dimension* (Oxford University Press, Oxford, 2004).
- [2] E. Dagotto and T. M. Rice, Surprises on the way from one- to two-dimensional quantum magnets: The ladder materials, *Science* **271**, 618 (1996).
- [3] E. Orignac and T. Giamarchi, Meissner effect in a bosonic ladder, *Phys. Rev. B* **64**, 144515 (2001).
- [4] J. Dalibard, F. Gerbier, G. Juzeliūnas, and P. Öhberg, Colloquium, *Rev. Mod. Phys.* **83**, 1523 (2011).
- [5] N. Goldman, G. Juzeliūnas, P. Öhberg, and I. B. Spielman, Light-induced gauge fields for ultracold atoms, *Rep. Prog. Phys.* **77**, 126401 (2014).
- [6] M. Atala, M. Aidelsburger, M. Lohse, J. T. Barreiro, B. Paredes, and I. Bloch, Observation of chiral currents with ultracold atoms in bosonic ladders, *Nat. Phys.* **10**, 588 (2014).
- [7] S. T. Carr, B. N. Narozhny, and A. A. Nersisyan, Spinless fermionic ladders in a magnetic field: Phase diagram, *Phys. Rev. B* **73**, 195114 (2006).
- [8] G. Roux, E. Orignac, S. White, and D. Poilblanc, Diamagnetism of doped two-leg ladders and probing the nature of their commensurate phases, *Phys. Rev. B* **76**, 195105 (2007).
- [9] A. Dhar, M. Maji, T. Mishra, R. V. Pai, S. Mukerjee, and A. Paramekanti, Bose-Hubbard model in a strong effective magnetic field: Emergence of a chiral Mott insulator ground state, *Phys. Rev. A* **85**, 041602(R) (2012).
- [10] A. Dhar, T. Mishra, M. Maji, R. V. Pai, S. Mukerjee, and A. Paramekanti, Chiral Mott insulator with staggered loop currents in the fully frustrated Bose-Hubbard model, *Phys. Rev. B* **87**, 174501 (2013).
- [11] A. Petrescu and K. Le Hur, Bosonic Mott Insulator with Meissner Currents, *Phys. Rev. Lett.* **111**, 150601 (2013).
- [12] R. Wei and E. J. Mueller, Theory of bosons in two-leg ladders with large magnetic fields, *Phys. Rev. A* **89**, 063617 (2014).
- [13] A. Tokuno and A. Georges, Ground states of a Bose-Hubbard ladder in an artificial magnetic field: Field-theoretical approach, *New J. Phys.* **16**, 073005 (2014).

- [14] M. Di Dio, S. De Palo, E. Orignac, R. Citro, and M.-L. Chiofalo, Persisting Meissner state and incommensurate phases of hard-core boson ladders in a flux, *Phys. Rev. B* **92**, 060506(R) (2015).
- [15] M. Piraud, F. Heidrich-Meisner, I. P. McCulloch, S. Greschner, T. Vekua, and U. Schollwöck, Vortex and Meissner phases of strongly interacting bosons on a two-leg ladder, *Phys. Rev. B* **91**, 140406(R) (2015).
- [16] S. Greschner, M. Piraud, F. Heidrich-Meisner, I. P. McCulloch, U. Schollwöck, and T. Vekua, Spontaneous Increase of Magnetic Flux and Chiral-Current Reversal in Bosonic Ladders: Swimming against the Tide, *Phys. Rev. Lett.* **115**, 190402 (2015).
- [17] A. Petrescu and K. Le Hur, Chiral Mott insulators, Meissner effect, and Laughlin states in quantum ladders, *Phys. Rev. B* **91**, 054520 (2015).
- [18] S. Uchino and A. Tokuno, Population-imbalance instability in a Bose-Hubbard ladder in the presence of a magnetic flux, *Phys. Rev. A* **92**, 013625 (2015).
- [19] S. Greschner, M. Piraud, F. Heidrich-Meisner, I. P. McCulloch, U. Schollwöck, and T. Vekua, Symmetry-broken states in a system of interacting bosons on a two-leg ladder with a uniform Abelian gauge field, *Phys. Rev. A* **94**, 063628 (2016).
- [20] S. Uchino, Analytical approach to a bosonic ladder subject to a magnetic field, *Phys. Rev. A* **93**, 053629 (2016).
- [21] E. Orignac, R. Citro, M. D. Dio, S. D. Palo, and M.-L. Chiofalo, Incommensurate phases of a bosonic two-leg ladder under a flux, *New J. Phys.* **18**, 055017 (2016).
- [22] A. Petrescu, M. Piraud, G. Roux, I. P. McCulloch, and K. Le Hur, Precursor of the Laughlin state of hard-core bosons on a two-leg ladder, *Phys. Rev. B* **96**, 014524 (2017).
- [23] M. Calvanese Strinati, E. Cornfeld, D. Rossini, S. Barbarino, M. Dalmonte, R. Fazio, E. Sela, and L. Mazza, Laughlin-like States in Bosonic and Fermionic Atomic Synthetic Ladders, *Phys. Rev. X* **7**, 021033 (2017).
- [24] E. Orignac, R. Citro, M. Di Dio, and S. De Palo, Vortex lattice melting in a boson ladder in an artificial gauge field, *Phys. Rev. B* **96**, 014518 (2017).
- [25] M. Calvanese Strinati, R. Berkovits, and E. Shimshoni, Emergent bosons in the fermionic two-leg flux ladder, *Phys. Rev. B* **100**, 245149 (2019).
- [26] M. Buser, F. Heidrich-Meisner, and U. Schollwöck, Finite-temperature properties of interacting bosons on a two-leg flux ladder, *Phys. Rev. A* **99**, 053601 (2019).
- [27] M. Buser, C. Hubig, U. Schollwöck, L. Tarruell, and F. Heidrich-Meisner, Interacting bosonic flux ladders with a synthetic dimension: Ground-state phases and quantum quench dynamics, *Phys. Rev. A* **102**, 053314 (2020).
- [28] X. Qiao, X.-B. Zhang, Y. Jian, A.-X. Zhang, Z.-F. Yu, and J.-K. Xue, Quantum phases of interacting bosons on biased two-leg ladders with magnetic flux, *Phys. Rev. A* **104**, 053323 (2021).
- [29] A. Haller, M. Rizzi, and M. Burrello, The resonant state at filling factor $\nu = 1/2$ in chiral fermionic ladders, *New J. Phys.* **20**, 053007 (2018).
- [30] A. Haller, A. S. Matsoukas-Roubeas, Y. Pan, M. Rizzi, and M. Burrello, Exploring helical phases of matter in bosonic ladders, *Phys. Rev. Res.* **2**, 043433 (2020).
- [31] S. Greschner, M. Filippone, and T. Giamarchi, Universal Hall Response in Interacting Quantum Systems, *Phys. Rev. Lett.* **122**, 083402 (2019).
- [32] M. Buser, S. Greschner, U. Schollwöck, and T. Giamarchi, Probing the Hall Voltage in Synthetic Quantum Systems, *Phys. Rev. Lett.* **126**, 030501 (2021).
- [33] M. Mancini, G. Pagano, G. Cappellini, L. Livi, M. Rider, J. Catani, C. Sias, P. Zoller, M. Inguscio, M. Dalmonte, and L. Fallani, Observation of chiral edge states with neutral fermions in synthetic Hall ribbons, *Science* **349**, 1510 (2015).
- [34] D. Genkina, L. M. Aycock, H.-I. Lu, M. Lu, A. M. Pineiro, and I. B. Spielman, Imaging topology of Hofstadter ribbons, *New J. Phys.* **21**, 053021 (2019).
- [35] T.-W. Zhou, G. Cappellini, D. Tusi, L. Franchi, J. Parravicini, C. Repellin, S. Greschner, M. Inguscio, T. Giamarchi, M. Filippone, J. Catani, and L. Fallani, Observation of universal Hall response in strongly interacting fermions, [arXiv:2205.13567](https://arxiv.org/abs/2205.13567).
- [36] T. Mishra, R. V. Pai, S. Mukerjee, and A. Paramekanti, Quantum phases and phase transitions of frustrated hard-core bosons on a triangular ladder, *Phys. Rev. B* **87**, 174504 (2013).
- [37] T. Mishra, R. V. Pai, and S. Mukerjee, Supersolid in a one-dimensional model of hard-core bosons, *Phys. Rev. A* **89**, 013615 (2014).
- [38] E. Anisimovas, M. Račiūnas, C. Sträter, A. Eckardt, I. B. Spielman, and G. Juzeliūnas, Semisynthetic zigzag optical lattice for ultracold bosons, *Phys. Rev. A* **94**, 063632 (2016).
- [39] F. A. An, E. J. Meier, and B. Gadway, Engineering a Flux-Dependent Mobility Edge in Disordered Zigzag Chains, *Phys. Rev. X* **8**, 031045 (2018).
- [40] F. A. An, E. J. Meier, J. Ang'ong'a, and B. Gadway, Correlated Dynamics in a Synthetic Lattice of Momentum States, *Phys. Rev. Lett.* **120**, 040407 (2018).
- [41] C. Romen and A. M. Läuchli, Chiral Mott insulators in frustrated Bose-Hubbard models on ladders and two-dimensional lattices: A combined perturbative and density matrix renormalization group study, *Phys. Rev. B* **98**, 054519 (2018).
- [42] S. Greschner and T. Mishra, Interacting bosons in generalized zigzag and railroad-trestle models, *Phys. Rev. B* **100**, 144405 (2019).
- [43] J. Cabedo, J. Claramunt, J. Mompert, V. Ahufinger, and A. Celi, Effective triangular ladders with staggered flux from spin-orbit coupling in 1D optical lattices, *Eur. Phys. J. D* **74**, 123 (2020).
- [44] Y. Li, H. Cai, D.-w. Wang, L. Li, J. Yuan, and W. Li, Many-Body Chiral Edge Currents and Sliding Phases of Atomic Spin Waves in Momentum-Space Lattice, *Phys. Rev. Lett.* **124**, 140401 (2020).
- [45] S. S. Roy, L. Carl, and P. Hauke, Genuine multipartite entanglement in one-dimensional Bose-Hubbard model with frustrated hopping, *Phys. Rev. B* **106**, 195158 (2022).
- [46] S. Wessel and M. Troyer, Supersolid Hard-Core Bosons on the Triangular Lattice, *Phys. Rev. Lett.* **95**, 127205 (2005).
- [47] C. Becker, P. Soltan-Panahi, J. Kronjaeger, S. Dörscher, K. Bongs, and K. Sengstock, Ultracold quantum gases in triangular optical lattices, *New J. Phys.* **12**, 065025 (2010).
- [48] J. Struck, C. Ölschläger, R. Le Targat, P. Soltan-Panahi, A. Eckardt, M. Lewenstein, P. Windpassinger, and K. Sengstock, Quantum simulation of frustrated classical magnetism in triangular optical lattices, *Science* **333**, 996 (2011).
- [49] A. Eckardt, P. Hauke, P. Soltan-Panahi, C. Becker, K. Sengstock, and M. Lewenstein, Frustrated quantum antiferromagnetism with ultracold bosons in a triangular lattice, *Europhys. Lett.* **89**, 10010 (2010).

- [50] M. P. Zaletel, S. A. Parameswaran, A. Rüegg, and E. Altman, Chiral bosonic Mott insulator on the frustrated triangular lattice, *Phys. Rev. B* **89**, 155142 (2014).
- [51] G. Vidal, J. I. Latorre, E. Rico, and A. Kitaev, Entanglement in Quantum Critical Phenomena, *Phys. Rev. Lett.* **90**, 227902 (2003).
- [52] P. Calabrese and J. Cardy, Entanglement entropy and quantum field theory, *J. Stat. Mech.: Theory Exp.* (2004) P06002.
- [53] C. Holzhey, F. Larsen, and F. Wilczek, Geometric and renormalized entropy in conformal field theory, *Nucl. Phys. B* **424**, 443 (1994).
- [54] I. Affleck and A. W. W. Ludwig, Universal Noninteger “Ground-State Degeneracy” in Critical Quantum Systems, *Phys. Rev. Lett.* **67**, 161 (1991).
- [55] N. Laflorencie, E. S. Sorensen, M.-S. Chang, and I. Affleck, Boundary Effects in the Critical Scaling of Entanglement Entropy in 1D Systems, *Phys. Rev. Lett.* **96**, 100603 (2006).
- [56] S. R. White, Density Matrix Formulation for Quantum Renormalization Groups, *Phys. Rev. Lett.* **69**, 2863 (1992).
- [57] U. Schollwöck, The density-matrix renormalization group, *Rev. Mod. Phys.* **77**, 259 (2005).
- [58] U. Schollwöck, The density-matrix renormalization group in the age of matrix product states, *Ann. Phys.* **326**, 96 (2011).
- [59] K. A. Hallberg, New trends in density matrix renormalization, *Adv. Phys.* **55**, 477 (2006).
- [60] E. Jeckelmann, Dynamical density-matrix renormalization-group method, *Phys. Rev. B* **66**, 045114 (2002).
- [61] M. Fishman, S. R. White, and E. M. Stoudenmire, The ITensor software library for tensor network calculations, *SciPost Phys. Codebases*, 4 (2022).
- [62] S. Greschner, L. Santos, and T. Vekua, Ultracold bosons in zigzag optical lattices, *Phys. Rev. A* **87**, 033609 (2013).
- [63] A. A. Nersisyan, A. O. Gogolin, and F. H. L. Eßler, Incommensurate Spin Correlations in Spin-1/2 Frustrated Two-Leg Heisenberg Ladders, *Phys. Rev. Lett.* **81**, 910 (1998).
- [64] S. Furukawa, M. Sato, and S. Onoda, Chiral Order and Electromagnetic Dynamics in One-Dimensional Multiferroic Cuprates, *Phys. Rev. Lett.* **105**, 257205 (2010).
- [65] S. Furukawa, M. Sato, S. Onoda, and A. Furusaki, Ground-state phase diagram of a spin- $\frac{1}{2}$ frustrated ferromagnetic XXZ chain: Haldane dimer phase and gapped/gapless chiral phases, *Phys. Rev. B* **86**, 094417 (2012).
- [66] H. Ueda and S. Onoda, Roles of easy-plane and easy-axis XXZ anisotropy and bond alternation in a frustrated ferromagnetic spin- $\frac{1}{2}$ chain, *Phys. Rev. B* **101**, 224439 (2020).
- [67] J. Struck, C. Ölschläger, M. Weinberg, P. Hauke, J. Simonet, A. Eckardt, M. Lewenstein, K. Sengstock, and P. Windpassinger, Tunable Gauge Potential for Neutral and Spinless Particles in Driven Optical Lattices, *Phys. Rev. Lett.* **108**, 225304 (2012).
- [68] M. Aidelsburger, M. Atala, S. Nascimbène, S. Trotzky, Y.-A. Chen, and I. Bloch, Experimental Realization of Strong Effective Magnetic Fields in an Optical Lattice, *Phys. Rev. Lett.* **107**, 255301 (2011).
- [69] H. Miyake, G. A. Siviloglou, C. J. Kennedy, W. C. Burton, and W. Ketterle, Realizing the Harper Hamiltonian with Laser-Assisted Tunneling in Optical Lattices, *Phys. Rev. Lett.* **111**, 185302 (2013).
- [70] M. E. Tai, A. Lukin, M. Rispoli, R. Schittko, T. Menke, D. Borgnia, P. M. Preiss, F. Grusdt, A. M. Kaufman, and M. Greiner, Microscopy of the interacting Harper-Hofstadter model in the two-body limit, *Nature (London)* **546**, 519 (2017).
- [71] T. Chalopin, T. Satoor, A. Evrard, V. Makhlov, J. Dalibard, R. Lopes, and S. Nascimbene, Probing chiral edge dynamics and bulk topology of a synthetic Hall system, *Nat. Phys.* **16**, 1017 (2020).
- [72] R. V. Roell, A. W. Laskar, F. R. Huybrechts, and M. Weitz, Chiral edge dynamics of cold erbium atoms in the lowest Landau level of a synthetic quantum Hall system, [arXiv:2210.09874](https://arxiv.org/abs/2210.09874).
- [73] M. Buser, U. Schollwöck, and F. Grusdt, Snapshot-based characterization of particle currents and the Hall response in synthetic flux lattices, *Phys. Rev. A* **105**, 033303 (2022).
- [74] C. Guo and D. Poletti, Geometry of system-bath coupling and gauge fields in bosonic ladders: Manipulating currents and driving phase transitions, *Phys. Rev. A* **94**, 033610 (2016).
- [75] C. Kollath, A. Sheikhan, S. Wolff, and F. Brennecke, Ultracold Fermions in a Cavity-Induced Artificial Magnetic Field, *Phys. Rev. Lett.* **116**, 060401 (2016).
- [76] C.-M. Halati, A. Sheikhan, and C. Kollath, Cavity-induced artificial gauge field in a Bose-Hubbard ladder, *Phys. Rev. A* **96**, 063621 (2017).
- [77] C.-M. Halati, A. Sheikhan, and C. Kollath, Cavity-induced spin-orbit coupling in an interacting bosonic wire, *Phys. Rev. A* **99**, 033604 (2019).
- [78] B. Xing, X. Xu, V. Balachandran, and D. Poletti, Heat, particle, and chiral currents in a boundary driven bosonic ladder in the presence of a gauge field, *Phys. Rev. B* **102**, 245433 (2020).
- [79] S. Lukyanov and A. Zamolodchikov, Exact expectation values of local fields in the quantum sine-Gordon model, *Nucl. Phys. B* **493**, 571 (1997).